The Astrophysical Journal Supplement Series, 222:7 (28pp), 2016 January doi:10.3847/0067-0049/222/1/7

PLANCK COLD CLUMPS IN THE λ ORIONIS COMPLEX. I. DISCOVERY OF AN EXTREMELY YOUNG CLASS 0 PROTOSTELLAR OBJECT AND A PROTO-BROWN DWARF CANDIDATE IN THE BRIGHT-RIMMED CLUMP PGCC G192.32–11.88

Tie Liu[1], Qizhou Zhang[2], Kee-Tae Kim[1], Yuefang Wu[3], Chang Won Lee[1,4], Jeong-Eun Lee[5], Ken'ichi Tatematsu[6], Minho Choi[1], Mika Juvela[7], Mark Thompson[8], Paul F. Goldsmith[9], Sheng-yuan Liu[10], Hirano Naomi[10], Patrick Koch[10], Christian Henkel[11,12], Patricio Sanhueza[6], JinHua He[13], Alana Rivera-Ingraham[14], Ke Wang[15], Maria R. Cunningham[16], Ya-Wen Tang[10], Shih-Ping Lai[17], Jinghua Yuan[18], Di Li[18,19], Gary Fuller[20], Miju Kang[1], Quang Nguyen Luong[6], Hauyu Baobab Liu[10], Isabelle Ristorcelli[21], Ji Yang[22], Ye Xu[22], Tomoya Hirota[6], Diego Mardones[23], Sheng-Li Qin[24], Huei-Ru Chen[10,16], Woojin Kwon[1], FanYi Meng[25], Huawei Zhang[3], Mi-Ryang Kim[1], and Hee-Weon Yi[5]

[1] Korea Astronomy and Space Science Institute, 776 Daedeokdae-ro, Yuseong-gu, Daejeon 34055, Korea; liutiepku@gmail.com
[2] Harvard-Smithsonian Center for Astrophysics, 60 Garden Street, Cambridge, MA 02138, USA
[3] Department of Astronomy, Peking University, 100871, Beijing, China
[4] University of Science & Technology, 217 Gajungro, Yuseong-gu, 305-333 Daejeon, Korea
[5] School of Space Research, Kyung Hee University, Yongin-Si, Gyeonggi-Do 446-701, Korea
[6] National Astronomical Observatory of Japan, 2-21-1 Osawa, Mitaka, Tokyo 181-8588, Japan
[7] Department of Physics, University of Helsinki, FI-00014 Helsinki, Finland
[8] Centre for Astrophysics Research, University of Hertfordshire, College Lane, Hatfield, AL10 9AB, UK
[9] Jet Propulsion Laboratory, California Institute of Technology, 4800 Oak Grove Drive, Pasadena, CA 91109, USA
[10] Academia Sinica, Institute of Astronomy and Astrophysics, P.O. Box 23-141, Taipei 106, Taiwan
[11] Max-Planck-Institut für Radioastronomie, Auf dem Hügel 69, D-53121, Bonn, Germany
[12] Astronomy Department, Abdulaziz University, P.O. Box 80203, 21589, Jeddah, Saudi Arabia
[13] Key Laboratory for the Structure and Evolution of Celestial Objects, Yunnan Observatories, Chinese Academy of Sciences, P.O. Box 110, Kunming, 650011, Yunnan Province, Pr China
[14] ESA/ESAC, E-28691 Villanueva de la Cañada, Madrid, Spain
[15] European Southern Observatory, Karl-Schwarzschild-Strasse 2, D-85748 Garching bei München, Germany
[16] School of Physics, University of New South Wales, Sydney, NSW 2052, Australia
[17] Institute of Astronomy and Department of Physics, National Tsing Hua University, Hsinchu, Taiwan
[18] National Astronomical Observatories, Chinese Academy of Sciences, Beijing, 100012, China
[19] Key Lab of Radio Astronomy, Chinese Academy of Sciences, China
[20] Jodrell Bank Centre for Astrophysics, Alan Turing Building, School of Physics and Astronomy, University of Manchester, Manchester M13 9PL, UK
[21] IRAP, CNRS (UMR5277), Université Paul Sabatier, 9 avenue du Colonel Roche, BP 44346, F-31028, Toulouse Cedex 4, France
[22] Purple Mountain Observatory, Chinese Academy of Sciences, Nanjing 210008, China
[23] Departamento de Astronomía, Universidad de Chile, Casilla 36-D, Santiago, Chile
[24] Department of Astronomy, Yunnan University, and Key Laboratory of Astroparticle Physics of Yunnan Province, Kunming, 650091, China
[25] Physikalisches Institut, Universität zu Köln, Zülpicher Strasse 77, D-50937 Köln, Germany
Received 2015 October 6; accepted 2015 November 24; published 2016 January 14

ABSTRACT

We are performing a series of observations with ground-based telescopes toward Planck Galactic cold clumps (PGCCs) in the λ Orionis complex in order to systematically investigate the effects of stellar feedback. In the particular case of PGCC G192.32–11.88, we discovered an extremely young Class 0 protostellar object (G192N) and a proto-brown dwarf candidate (G192S). G192N and G192S are located in a gravitationally bound bright-rimmed clump. The velocity and temperature gradients seen in line emission of CO isotopologues indicate that PGCC G192.32–11.88 is externally heated and compressed. G192N probably has the lowest bolometric luminosity (~0.8 $L_{\odot}$) and accretion rate (6.3 × 10^{-7} $M_{\odot}$ yr^{-1}) when compared with other young Class 0 sources (e.g., PACS Bright Red Sources) in the Orion complex. It has slightly larger internal luminosity (0.21 ± 0.01 $L_{\odot}$) and outflow velocity (~14 km s^{-1}) than the predictions of first hydrostatic cores (FHSCs). G192N might be among the youngest Class 0 sources, which are slightly more evolved than an FHSC. Considering its low internal luminosity (0.08 ± 0.01 $L_{\odot}$) and accretion rate (2.8 × 10^{-8} $M_{\odot}$ yr^{-1}), G192S is an ideal proto-brown dwarf candidate. The star formation efficiency (~0.3%–0.4%) and core formation efficiency (~1%) in PGCC G192.32–11.88 are significantly smaller than in other giant molecular clouds or filaments, indicating that the star formation therein is greatly suppressed owing to stellar feedback.

Key words: ISM: jets and outflows – ISM: kinematics and dynamics – stars: formation

1. INTRODUCTION

Stellar feedback from massive stars can strongly influence their surrounding interstellar medium (ISM) and regulate star formation through outflows, photoionizing radiation, energetic winds, and supernova explosions. Such stellar feedback may have both "negative" and "positive" effects on molecular clouds (Dale et al. 2015). In the negative aspect, expanding H II regions or supernova explosions are energetic enough to sweep up the surrounding molecular gas and destroy giant molecular clouds (GMCs). Stellar feedback might also be responsible for the low star formation efficiencies (SFEs) or low star formation rates (SFRs) in GMCs (Solomon et al. 1979;

Dale et al. 2012, 2013). However, whether the low SFE and SFR in GMCs are caused by stellar feedback is still under debate. For example, most nearby GMCs uniformly have low SFEs (Evans et al. 2009). While it has been stated that there are no obvious signs of stellar feedback such as bubbles (Krumholz et al. 2014), more recent studies suggest that bubbles are prevalent around even low-mass young stellar objects (YSOs) when inspected closely (Arce et al. 2011; Li et al. 2015).

The positive aspect of stellar feedback is usually referred to as triggered star formation. The shock front (SF) that emerges as bubbles around massive stars expand can compress the ISM, triggering star formation in very dense layers (Chen et al. 2007). Thompson et al. (2012) discovered an enhanced surface density of YSOs projected against the rim of infrared bubbles, suggesting that the YSOs were triggered by the expansion of the bubbles. They also estimated that the fraction of massive stars in the Milky Way formed by the triggering process could be between 14% and 30% (Thompson et al. 2012). Theoretically, the ionization front (IF) generated from an H II region can generate an SF in molecular clouds and gather molecular gas to form a dense shell between the IF and the SF (Elmegreen & Lada 1977; Whitworth et al. 1994). The gas and dust in the collected layer collapse to form stars when they reach the critical density (Whitworth et al. 1994; Chen et al. 2007; Ogura 2010). This so-called "collect and collapse" process can self-propagate and lead to sequential star formation (Elmegreen & Lada 1977; Whitworth et al. 1994). Star formation induced through the "collect and collapse" process has been revealed in the borders of several H II regions evidenced by fragmented shells or sequential star formation (Deharveng et al. 2003, 2005; Zavagno et al. 2006, 2007; Deharveng et al. 2008; Pomarès et al. 2009; Petriella et al. 2010; Brand et al. 2011; Liu et al. 2012b, 2015). Another model for triggered star formation is the so-called "radiation-driven implosion" (RDI; Bertoldi & McKee 1990; Lefloch & Lazareff 1994; Ogura 2010), in which the surface layer of a preexisting cloud is ionized by the UV photons from nearby massive stars and then the cloud is compressed and collapsed owing to the shock generated from the IF. The difference between the "collect and collapse" and the RDI processes is whether the molecular cloud is collected as the IF advances or is preexisting before the bubble expands. Bright-rimmed clouds are often treated as a hint of triggered star formation due to the RDI process because their rims are the glowing ionized boundary layers on the irradiated faces of the clouds. Candidates for star formation by RDI have been suggested in many bright-rimmed clouds (Sugitani et al. 1991; Sugitani & Ogura 1994; Thompson et al. 2004; Urquhart et al. 2004; Lee et al. 2005; Urquhart et al. 2006, 2007; Morgan et al. 2010; Liu et al. 2012b).

However, recent numerical simulations indicate that most signs in previous observational works, such as the ages and geometrical distribution of stars relative to the feedback source or feedback-driven structure (e.g., shells, pillar structures), are not substantially helpful in distinguishing triggered star formation from spontaneous star formation (Dale et al. 2015). Triggered star formation can increase either the SFR, the SFE, or the total numbers of stars formed (Dale et al. 2015). Therefore, to trace triggered star formation, we need to carefully investigate how molecular clouds interact with feedback sources (H II regions or supernova remnants) and how the SFR and SFE change in molecular clouds owing to stellar feedback.

The λ Orionis complex contains one of the most prominent OB associations in Orion. As shown in the left panel of Figure 1, it is a giant H II region with a ring-like structure of dust and gas of $8^\circ-10^\circ$ in diameter (Maddalena & Morris 1987; Zhang et al. 1989; Dolan & Mathieu 2002). The central λ Ori cluster contains a (O8 III) massive star with a massive companion that became a supernova (Maddalena & Morris 1987; Cunha & Smith 1996; Dolan & Mathieu 2002), removing nearby molecular gas at the center of the cluster about 1 Myr ago and leading to the formation of the ring of dust and gas (Mathieu 2008). As one of the nearest large H II regiosn, the λ Orionis complex is an ideal laboratory for studies of stellar feedback. In this region, the age sequence of classical T Tauri stars (CTTSs) and the high SFE of some bright-rimmed clouds (e.g., B35 and LDN 1634) provide strong evidence of triggered star formation (Lee et al. 2005). However, the properties (e.g., substructures, gravitational stability) of molecular clouds in the λ Orionis complex are far from well understood owing to a lack of high angular resolution observations in both molecular lines and (sub)millimeter continuum.

Planck is the third generation mission to measure the anisotropy of the cosmic microwave background (CMB) and observed the sky in nine frequency bands (the 30, 44, 70, 100, 143, 217, 353, 545, and 857 GHz bands). The high-frequency channels of *Planck* cover the peak thermal emission frequencies of dust colder than 14 K, indicating that *Planck* could probe the coldest parts of the ISM (Planck Collaboration et al. 2011, 2015). The Planck team has cataloged 13,188 Planck galactic cold clumps (PGCCs; Planck Collaboration et al. 2015). Having low dust temperatures of 6–20 K, Planck cold clumps show the smallest line widths but modest column densities when compared to other kinds of star-forming clouds (Planck Collaboration et al. 2011, 2015; Wu et al. 2012; Liu et al. 2013, 2014). A large fraction of PGCCs seem to be quiescent, not affected by ongoing star-forming activities, suggesting that they might trace very initial conditions of star formation (Wu et al. 2012; Liu et al. 2013, 2014; Tóth et al. 2014). Planck cold clumps are highly structured, as indicated in Herschel follow-up observations (Juvela et al. 2012) and mapping observations in CO isotopologues with the Purple Mountain Observatory (PMO) 13.7 m telescope (Liu et al. 2012a; Meng et al. 2013; Liu et al. 2014). There are about 180 PGCCs located in the λ Orionis complex. As shown in the left panel of Figure 1, most of the densest PGCCs with a clump-averaged column density larger than 5×10^{20} cm^{-2} are located in the rim of the H II region. Therefore, the studies of PGCCs in the λ Orionis complex will provide us with information on how the stellar feedback of the H II region influences the initial conditions of star formation. To improve our understanding of star formation in the λ Orionis complex, we are conducting a series of observations toward Planck cold clumps with several ground-based telescopes (see Section 2 for details).

Here we report the first results from our observations toward a particular source, PGCC G192.32–11.88, which is located in the B30 cloud of the λ Orionis complex. It has a size of $\sim 11\farcm2 \times 4\farcm5$, with the long axis parallel to the Galactic plane (Planck Collaboration et al. 2015). The cold component has a clump-averaged temperature of 17.3 ± 6.0 K (Planck

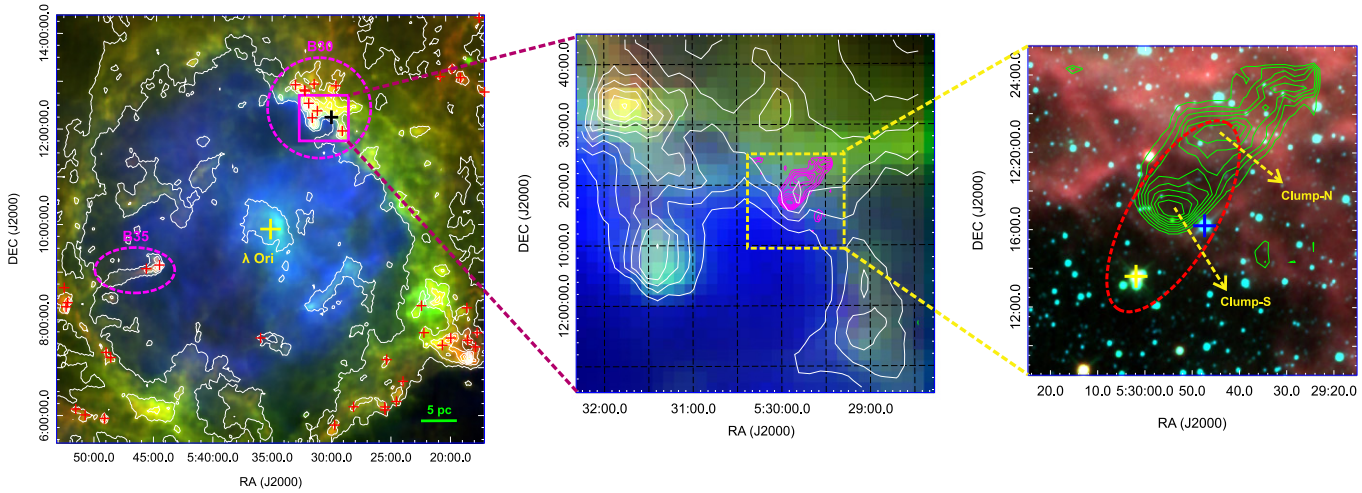

Figure 1. Left panel: three-color composite image (red: Planck 857 GHz; green: IRAS 100 μm; blue: Hα) of the λ Orionis complex. The white contours represent the flux density of Planck 857 GHz continuum emission. The contours are from 10% to 90% in steps of 10% of peak value 133.1 MJy sr^{-1}. The two bright-rimmed clouds B30 and B35 are marked with pink ellipses. The "λ Ori" OB binary- or multiple-star system is marked with a yellow plus sign. PGCC G192.32–11.88 is marked with a black plus sign. All Planck cold clumps in this region with a clump-averaged column density larger than 5×10^{20} cm^{-2} are shown as red plus signs. Middle panel: environment of PGCC G192.32–11.88. The color image and white contours are the same as in the left panel. The H_2 column density calculated from ^{13}CO (1–0) emission (see Section 3.1.3) of PGCC G192.32–11.88 is shown in pink contours. The contour levels are from 20% to 90% in steps of 10% of the peak value 1.22×10^{22} cm^{-2}. Right panel: H_2 column density calculated from CO isotopologues is shown in green contours overlayed on the *WISE* three-color composite image (3.4 μm in blue, 4.6 μm in green, 22 μm in red). The contours are the same as in the middle panel. The dashed ellipse marks the shape of PGCC G192.32–11.88. The B-type star HD 36104 is marked with a blue plus sign. The nearby multiple-star system, which contains four variable stars (VGX Ori, V V370 Ori, V V443 Ori, and VV444 Ori) of Orion type, is marked with a yellow plus sign. The two main gas clumps "Clump-N" and "Clump-S" are marked with yellow dashed arrows.

Collaboration et al. 2015), while the warm background has a dust temperature of 28.1 ± 4.4 K (Planck Collaboration et al. 2015). As shown in the middle panel of Figure 1, PGCC G192.32–11.88 as a bright-rimmed clump is facing the H II region and is surrounded by Hα emission, indicating that it is shaped by the photo-erosion of the ionizing radiation. It contains two main gas clumps, "Clump-N" and "Clump-S," as revealed in ^{13}CO (1–0) emission in the right panel of Figure 1. The B-type star HD 36104 is at the southwest edge of "Clump-S." The distance of the λ Orionis complex is in between 380 ± 30 pc, as derived by *Hipparcos*, and 420 ± 42 pc, as derived from Pan-STARRS1 photometry (Schlafly et al. 2014). However, different clouds in the λ Orionis complex might have various distances from ~380 to ~470 pc (Schlafly et al. 2014). The distance of the B-type star HD 36104 close to PGCC G192.32–11.88 is 364 ± 32 pc as derived by *Hipparcos* (Dolan & Mathieu 2001). In this paper we adopt a distance of 380 pc for PGCC G192.32–11.88. PGCC G192.32–11.88 only has a mass of 3.0 ± 2.4 $M_\odot$, as inferred from the *Planck* data at a distance of 380 pc.

2. OBSERVATIONS

2.1. PMO 13.7 m Telescope Observations

The observations toward PGCC G192.32–11.88 in the ^{12}CO (1–0), ^{13}CO (1–0), and C^{18}O (1–0) lines were carried out with the PMO 13.7 m radio telescope in 2011 May. The new nine-beam array receiver system in single-sideband mode was used as the front end (Shan et al. 2012). FFTS spectrometers were used as back ends, which have a total bandwidth of 1 GHz and 16,384 channels, corresponding to a velocity resolution of 0.16 km s^{-1} for the ^{12}CO (1–0) and 0.17 km s^{-1} for the ^{13}CO (1–0) and the C^{18}O (1–0). The ^{12}CO (1–0) was observed in the upper sideband (USB), while the ^{13}CO (1–0) and the C^{18}O (1–0) were observed simultaneously in the lower sideband (LSB). The half-power beam width (HPBW) is 56″, and the main-beam efficiency is ~0.45. The pointing accuracy of the telescope was better than 4″. The typical system temperatures ($T_{\rm sys}$) are around 130 K for LSB and 220 K for USB, which vary about 10% among the nine beams. The on-the-fly (OTF) observing mode was utilized. The antenna continuously scanned a region of 22′ × 22′ centered on the Planck cold clumps with a scan speed of 20″ s^{-1}. However, the edges of the OTF maps have a much higher noise level, and thus only the central 14′ × 14′ regions are selected to be further analyzed. The typical rms noise level per channel was 0.3 K in T_A^* for the ^{12}CO (1–0) and 0.2 K for the ^{13}CO (1–0) and the C^{18}O (1–0).

2.2. CSO 10 m Telescope Observations

Observations of "Clump-S" in the ^{12}CO (2–1), ^{13}CO (2–1), and C^{18}O (2–1) lines were carried out with the Caltech Submillimeter Observatory (CSO) 10 m radio telescope in 2014 January. We used the Sidecab receiver and the FFTS2 spectrometer. The spectral resolution is ~0.35 km s^{-1}. The weather was good during observations with a system temperature of 244 K. The beam size and beam efficiency of the CSO telescope at 230 GHz are ~34″ and 0.76, respectively. The map size is 5′ × 5′, with a spacing of 10″. The typical rms noise level per channel is 0.2 K in T_A^*.

Using the GILDAS software package including CLASS and GREG (Guilloteau et al. 2000), the OTF data of CO isotopologues were converted to 3D cube data. Baseline subtraction was performed by fitting linear or sinusoidal functions. Then the data were exported to MIRIAD (Sault et al. 1995) and CASA for further analysis.

2.3. KVN 21 m Telescope Observations

We also observed "Clump-S" in the $J = 1$–0 transitions of HCO$^+$, H^{13}CO$^+$, and N_2H^+, as well as HDCO ($2_{0,2} - 1_{0,1}$) and o-H_2CO ($2_{1,2} - 1_{1,1}$), with the Korean VLBI Network (KVN) 21 m telescope at Yonsei station in single-dish mode (Kim

et al. 2011). The observations were carried out in 2015 February. The spectral resolution and system temperature for the $J = 1$–0 of HCO^+, $H^{13}CO^+$, and N_2H^+ (1–0) are $\sim$0.052 km s^{-1} and 230 K, respectively. The spectral resolution and system temperature for HDCO ($2_{0,2} - 1_{0,1}$) and o-H_2CO ($2_{1,2} - 1_{1,1}$) are $\sim$0.034 km s^{-1} and 453 K, respectively. We did single-pointing observations with an rms level per channel of $T_A^* < 0.1$ K. The beam size and beam efficiency of the KVN telescope at 86 GHz band are $\sim$32″ and 0.41, respectively. The beam size and beam efficiency of the KVN telescope in the 129 GHz band are $\sim$24″ and 0.40, respectively. The data were reduced using the GILDAS software package.

2.4. JCMT 15 m Telescope Observations

The observations of "Clump-S" with James Clerk Maxwell Telescope (JCMT) SCUBA-2 were conducted in 2015 April. We used the "CV Daisy" mapping mode, which is suitable for point sources. The 225 GHz opacity during observations ranges from 0.088 to 0.11. Therefore, we only obtained 850 μm continuum data. The data were reduced using SMURF in the STARLINK package. The FOV of SCUBA-2 at 850 μm is 8′. The mapping area is about 12′ × 12′. The beam size of SCUBA-2 at 850 μm is $\sim$14″. The rms level in the central 3′ area of the map is around 8 mJy beam^{-1}.

2.5. The SMA Observations

The observations of "Clump-S" with the Submillimeter Array (SMA)[26] were carried out in 2014 November in its compact configuration. The phase reference center was R.A. (J2000) = 05^{h}29^{m}54^s.32 and decl. (J2000) = 12°16′40″.50. In observations, QSOs 0530 + 135 and 0510 + 180 were observed for gain and phase correction. QSO 3c 279 was used for bandpass calibration. Uranus was applied for flux-density calibration. The channel spacing across the 8 GHz spectral band is 0.812 MHz, or $\sim$1.1 km s^{-1}. The visibility data were calibrated with the IDL superset MIR package and imaged with the MIRIAD and CASA packages. The 1.3 mm continuum data were acquired by averaging all the line-free channels over both the upper and lower spectral bands. The synthesized beam size and 1σ rms of the continuum emission are 3.″4 × 2.″3 (PA = −59°) and $\sim$1 mJy beam^{-1}, respectively. The 1σ rms for lines is $\sim$50 mJy beam^{-1} per channel. We detect strong ^{12}CO (2–1) emission and weak ^{13}CO (2–1) emission above the 3σ signal-to-noise level in the SMA observations. To recover the missing flux in the SMA ^{12}CO (2–1) and ^{13}CO (2–1) emission, we combined the SMA data with the CSO data following a procedure outlined in Zhang et al. (1995). The combined SMA+CSO data for ^{12}CO (2–1) and ^{13}CO (2–1) emissions were convolved with the same beam size of 5.″2 × 3.″8 (PA = −53°) to derive the ^{13}CO column density. The 1σ rms for lines is $\sim$300 mJy beam^{-1} per channel in the SMA+CSO combined data. We use primary-beam-corrected continuum and line data in further analysis.

We also used *Spitzer* MIPS and IRAC archival data.

[26] The SMA is a joint project between the Smithsonian Astrophysical Observatory and the Academia Sinica Institute of Astronomy and Astrophysics and is funded by the Smithsonian Institution and the Academia Sinica (Ho et al. 2004).

3. RESULTS OF SINGLE-DISH OBSERVATIONS

3.1. Overall Properties of PGCC G192.32–11.88 Inferred from the Observations of CO Isotopologues

3.1.1. Moment Maps

The integrated intensity of ^{13}CO (1–0) is shown as contours overlayed on its Moment 1 color image in panel (a) of Figure 2. Two large clumps ("Clump-N" and "Clump-S") are revealed in ^{13}CO (1–0) emission. The integrated intensity of ^{13}CO (2–1) of "Clump-S" is shown as contours overlayed on its Moment 1 color image in panel (b) of Figure 2. From the Moment 1 maps, a clear velocity gradient is seen along the southwest to northeast direction, indicating that the cloud might be externally compressed. We derived the systemic velocities of ^{13}CO (1–0) and ^{13}CO (2–1) from Gaussian fits of the spectra along the dashed lines in panels (a) and (b) and plotted the position–velocity diagrams in panels (c) and (d), respectively. The velocities linearly decrease from the southwest to northeast. The direction of the velocity gradient is inconsistent with the elongation of the cloud. We notice that the B-type star HD 36104 is at the southwest edge of "Clump-S." Therefore, the velocity gradient may be caused by the joint effect of the radiation pressure from the giant H II region and HD 36104. From linear fits, we found that the velocity gradient of the cloud is 1.6–1.8 km s^{-1} pc^{-1}.

In Figure 3, we present the Moment 2 maps of ^{13}CO (1–0) and ^{13}CO (2–1) emission. The velocity dispersions become larger toward the clump centers, suggesting that the line widths might be broadened by feedback of star formation activity (e.g., outflows) inside the clumps.

3.1.2. Line Intensity Ratios

The integrated intensity ratios of ^{12}CO $J = 2$–1 to $J = 1$–0 (R_{12CO}) and ^{13}CO $J = 2$–1 to $J = 1$–0 (R_{13CO}) were calculated by convolving the ^{12}CO (2–1) and ^{13}CO (2–1) data with the beam of PMO 13.7 m. The two ratios are shown in color images in panels (a) and (b) of Figure 4. The ratios become larger from clump center to clump edge. The integrated intensity ratios of ^{12}CO (1–0) to ^{13}CO (1–0) ($R^{10}_{12CO/13CO}$) and ^{12}CO (2–1) to ^{13}CO (2–1) ($R^{21}_{12CO/13CO}$) were also derived and displayed in panels (c) and (d), respectively. Smaller $R^{10}_{12CO/13CO}$ and $R^{21}_{12CO/13CO}$ ratios indicate higher optical depths for CO emission. The optical depth of CO emission decreases from clump center to clump edge. In Table 1, we present statistical results of these ratios and integrated intensity of ^{13}CO and C^{18}O within a 50% contour (region 1), 20% contour of C^{18}O (1–0) (region 2), and 20% contour of ^{13}CO (1–0) (region 3), respectively. These statistical results are not artificial owing to low signal-to-noise level because the minimum value of ^{13}CO (2–1) integrated intensity within its 20% contour is 1.21 K km s^{-1}, which is larger than 6σ ($\sigma \sim 0.2$ K km s^{-1}). In general, the average density from region 1 to region 3 decreases, while the mean or maximum values of different ratios generally increase with decreasing average density, which quantitatively indicates that the CO emission at the clump edge is less optically thick and more highly excited than that at the clump center.

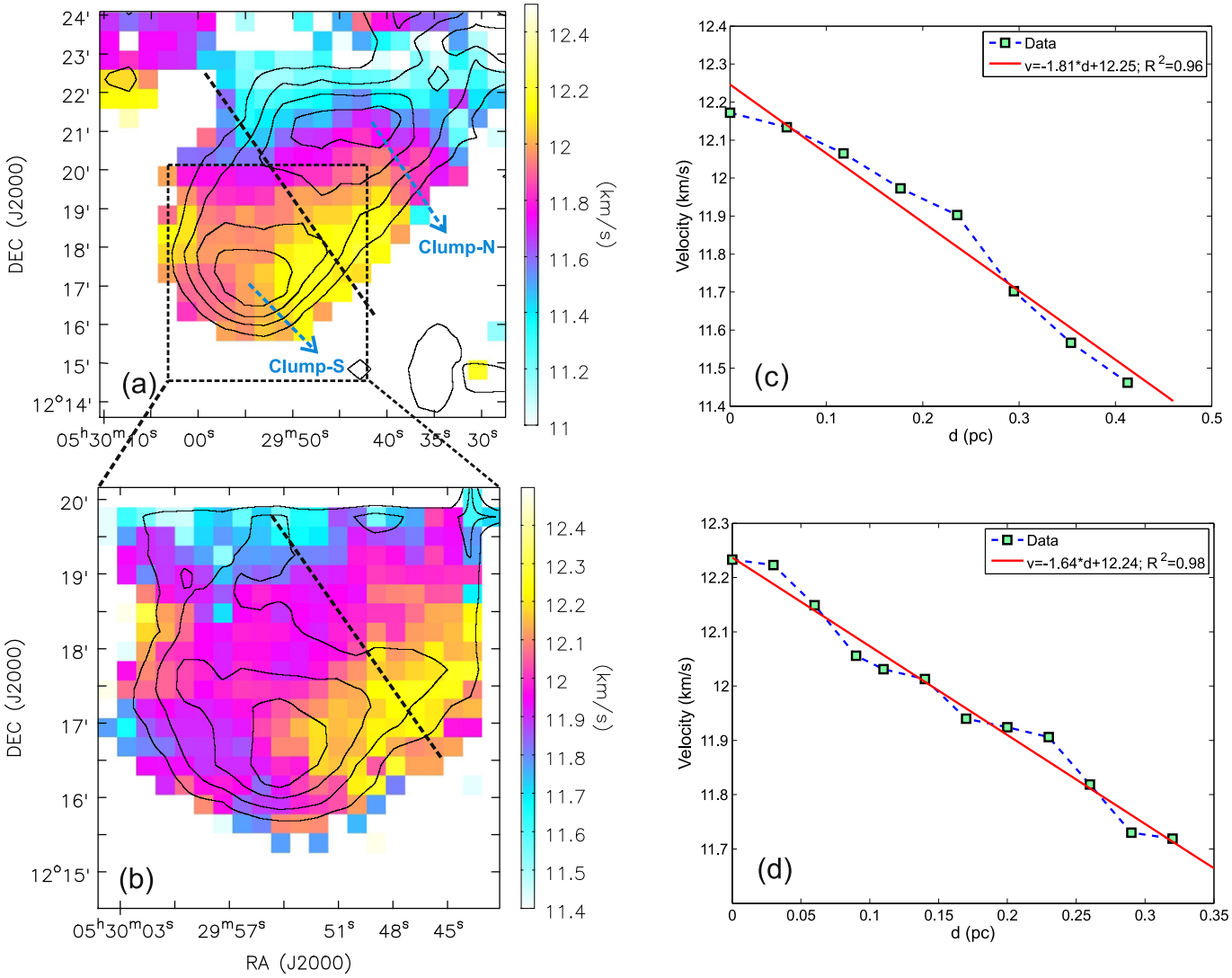

Figure 2. The black contours in panels (a) and (b) represent the integrated intensity of ^{13}CO (1–0) and ^{13}CO (2–1), respectively. The contour levels are from 20% to 80% in steps of 20% of the peak values. The peak values for ^{13}CO (1–0) and ^{13}CO (2–1) are 10.8 and 13.0 K km s^{-1}, respectively. Color images in panels (a) and (b) show the Moment 1 maps of ^{13}CO (1–0) and ^{13}CO (2–1), respectively. Panels (c) and (d) show the position–velocity diagrams of ^{13}CO (1–0) and ^{13}CO (2–1) along the dashed lines in panels (a) and (b), respectively. The distances were calculated from the southwest edge of the clump. The Moment 1 maps are constructed from the data after imposing a cutoff of 5σ.

3.1.3. Clump Properties from Local Thermodynamic Equilibrium (LTE) Analysis

We first calculated the excitation temperature of ^{12}CO (1–0) and column density of ^{13}CO assuming LTE. The details of the LTE analysis are described in Appendix A.

The mean peak brightness temperature ratio of ^{12}CO (1–0) to ^{13}CO (1–0) within the 20% contour of ^{13}CO (1–0) integrated intensity is ~4, corresponding to an optical depth of 17 for ^{12}CO (1–0) emission. Thus, ^{12}CO (1–0) emission is apparently optically thick in PGCC G192.32–11.88. The excitation temperature of ^{12}CO (1–0) is shown as a color image in Figure 5. It can be seen that the excitation temperature (T_{ex} ~ 21 K) at the western edge is higher than that (~15 K) at the eastern edge of the cloud, indicating that the cloud might be externally heated. The mean excitation temperatures of "Clump-S" and "Clump-N" are 18.1 ± 0.3 and 18.0 ± 0.2 K, respectively, which are consistent with the dust temperature (17.3 ± 6.0 K) of the cold component in *Planck* observations (Planck Collaboration et al. 2015).

The column density of H_2 was obtained by adopting typical abundance ratios $[H_2]/[^{12}CO] = 10^4$ and $[^{12}CO]/[^{13}CO] = 60$ in the ISM (Deharveng et al. 2008). The column density of H_2 is shown as contours in Figure 5. The mean column densities of "Clump-S" and "Clump-N" are (6.5 ±0.4) × 10^{21} and (6.3 ±0.2) × 10^{21} cm^{-2}, respectively.

The radii of the clumps are defined as $R = \sqrt{a \cdot b}$, where a and b are the FWHM deconvolved sizes of the major and minor axes, respectively. The radii of "Clump-S" and "Clump-N" are 0.33 and 0.47 pc, respectively. The LTE masses of the clumps are estimated as $M_{LTE} = \pi R^2 \cdot \overline{N} \cdot m_H \cdot \mu_g$, where $\overline{N}$ is the mean column density, m_H is the mass of atomic hydrogen, and $\mu_g = 2.8$ is the mean molecular weight of the gas. The LTE masses of "Clump-S" and "Clump-N" are 49 ± 3 and 99 ± 3 $M_\odot$, respectively. In calculating masses, we only considered the errors in flux measurement. Other uncertainties such as distance, abundance, and calibration were not taken into account. These systematic uncertainties can have an effect that is much greater than the random noise in the data

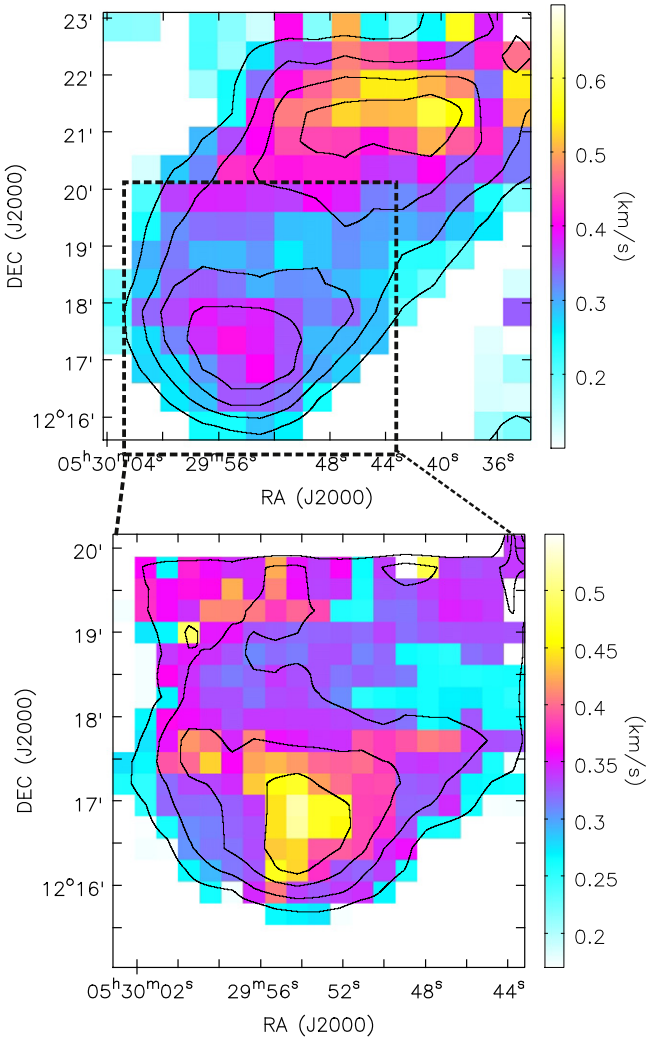

Figure 3. Color images show the Moment 2 maps of ^{13}CO (1–0) and ^{13}CO (2–1), respectively. The velocity dispersions become larger toward the clump centers, suggesting that the line widths might be broadened by feedback of star formation activity (e.g., outflows) inside the clumps. The black contours in the upper and lower panels represent integrated intensity of ^{13}CO (1–0) and ^{13}CO (2–1), respectively. The contour levels are the same as in Figure 2. The Moment 2 maps are constructed from the data after imposing a cutoff of 5σ.

on mass measurement. For example, the various distance determinations have uncertainties of approximately 10%. If the distance was actually 10% higher, then the LTE mass determination would be increased by ~20%. Additionally, as discussed in Section 3.3.1, CO gas may be depleted in the central region. Therefore, the abundance we adopted here might be larger than the real value. If we adopt an abundance two times smaller than the present value, the corresponding LTE masses will increase by a factor of 2. To study the gravitational stability of these two clumps, we also estimated their virial masses. The virial mass considering turbulent support can be derived as $\frac{M_{\rm vir}}{M_\odot} = 210(\frac{R}{\rm pc})(\frac{\Delta V}{\rm km\ s^{-1}})^2$(Zhang et al. 2015), where ΔV is the line width of C^{18}O (1–0). We used the C^{18}O (1–0) line rather than the ^{13}CO (1–0) line to derive virial masses because the C^{18}O (1–0) line emission is more optically thin than the ^{13}CO (1–0) line emission and therefore a better tracer for turbulence. From Gaussian fits toward the spectra at clump centers, the line widths of C^{18}O (1–0) of "Clump-S" and "Clump-N" are 0.93 ± 0.09 and 0.86 ± 0.11 km s^{-1}, respectively. Thus, the virial masses of "Clump-S" and "Clump-N" are 59 ± 10 and 74 ± 19 $M_\odot$, respectively. The virial masses of the two clumps are consistent with their LTE masses, indicating that these two gas clumps are gravitationally bound.

3.1.4. CO Gas Excitation from Non-LTE Analysis

In Figure 6, we applied RADEX (Van der Tak et al. 2007), a one-dimensional non-LTE radiative transfer code, to investigate the excitation of CO isotopologues within the 50% contour of C^{18}O (1–0) in "Clump-S" by exploring parameter ranges of H_2 volume density in $[1 \times 10^3,\ 5 \times 10^4]$ cm^{-3}, kinetic temperature in [15, 30] K, and column density of ^{12}CO in $[1 \times 10^{17},\ 5 \times 10^{18}]$ cm^{-2}. The modeled values, which are consistent with observed mean values within 1σ, are adopted. For example, the blue boxes in Figure 6 represent the solutions in which modeled $R_{\rm 13CO}$ is consistent with the observed value 1.04 ± 0.13. The best solutions should satisfy the criteria that all the modeled ratios ($R_{\rm 12CO}$, $R_{\rm 13CO}$, $R^{10}_{\rm 12CO/13CO}$, $R^{21}_{\rm 12CO/13CO}$) are consistent with the observed values. The kinetic temperature, volume density, and CO column density in the overlapped regions are 18.9 K, 3.2×10^3 cm^{-3}, and 1.05×10^{18} cm^{-2}, respectively, which are the best solutions. The kinetic temperature (18.9 K) is consistent with the average excitation temperature (18.84 ± 0.79 K) of ^{12}CO (1–0) in the LTE analysis, as listed in Table 1. Assuming an abundance ratio of $[H_2]/[^{12}CO] = 10^4$, the H_2 column density calculated with RADEX is 1.05×10^{22} cm^{-2}, which is the same as the value ($(1.05 \pm 0.18) \times 10^{22}$ cm^{-2}) obtained from the LTE analysis, suggesting that the central part of the southern clump satisfies the LTE condition very well. The thickness (h) of "Clump-S" can be estimated as $h = \frac{\overline{N_{\rm H_2}}}{\overline{n_{\rm H_2}}}$, where $\overline{N_{\rm H_2}}$ and $\overline{n_{\rm H_2}}$ are the average column density and volume density, respectively. The thickness of the clump is ~0.95 pc, which is about 1.5 times larger than the diameter (0.66 pc) of the southern clump.

In Figure 7, we investigate integrated intensity ratios versus kinetic temperature in three groups of volume density and column density. Roughly speaking, for a given density, integrated intensity ratios increase with kinetic temperature except for $R_{\rm 12CO}$ in the lowest-density group ($n_{\rm H_2} = 1.6 \times 10^3$ cm^{-3}). For a given kinetic temperature, $R^{10}_{\rm 12CO/13CO}$ and $R^{21}_{\rm 12CO/13CO}$ decrease with increasing density, indicating that in high-density regions CO is more optically thick. As shown in panels (c) and (d), extremely high ratios of $R^{10}_{\rm 12CO/13CO}$ and $R^{21}_{\rm 12CO/13CO}$ indicate much higher temperature and lower density. As shown in Table 1, the maximum values of $R_{\rm 12CO}$, $R_{\rm 13CO}$, $R^{10}_{\rm 12CO/13CO}$, and $R^{21}_{\rm 12CO/13CO}$ within the 20% contour of ^{13}CO (1–0) are 1.14, 2.27, 8.14, and 10.10, respectively. Such high ratios are larger than the maximum ratios we calculated with RADEX, as marked with black solid lines in Figure 7, indicating that the kinetic temperature should be larger than 50 K close to the clump edge. However, the $J = 1$ and 2 levels of CO are only at 5.53 K and 16.60 K above ground level, respectively, indicating that we could not reveal such high-temperature ($T_k > 50$ K) conditions accurately with the present data. Observations of higher J transitions of CO are needed to reveal the exact excitation condition at the clump edge. As shown in panels (c) and (d), to achieve extremely high $R^{10}_{\rm 12CO/13CO}$ and $R^{21}_{\rm 12CO/13CO}$, not only higher temperatures but also lower densities are needed, indicating that the clump might be surrounded by a hot and low-density envelope.

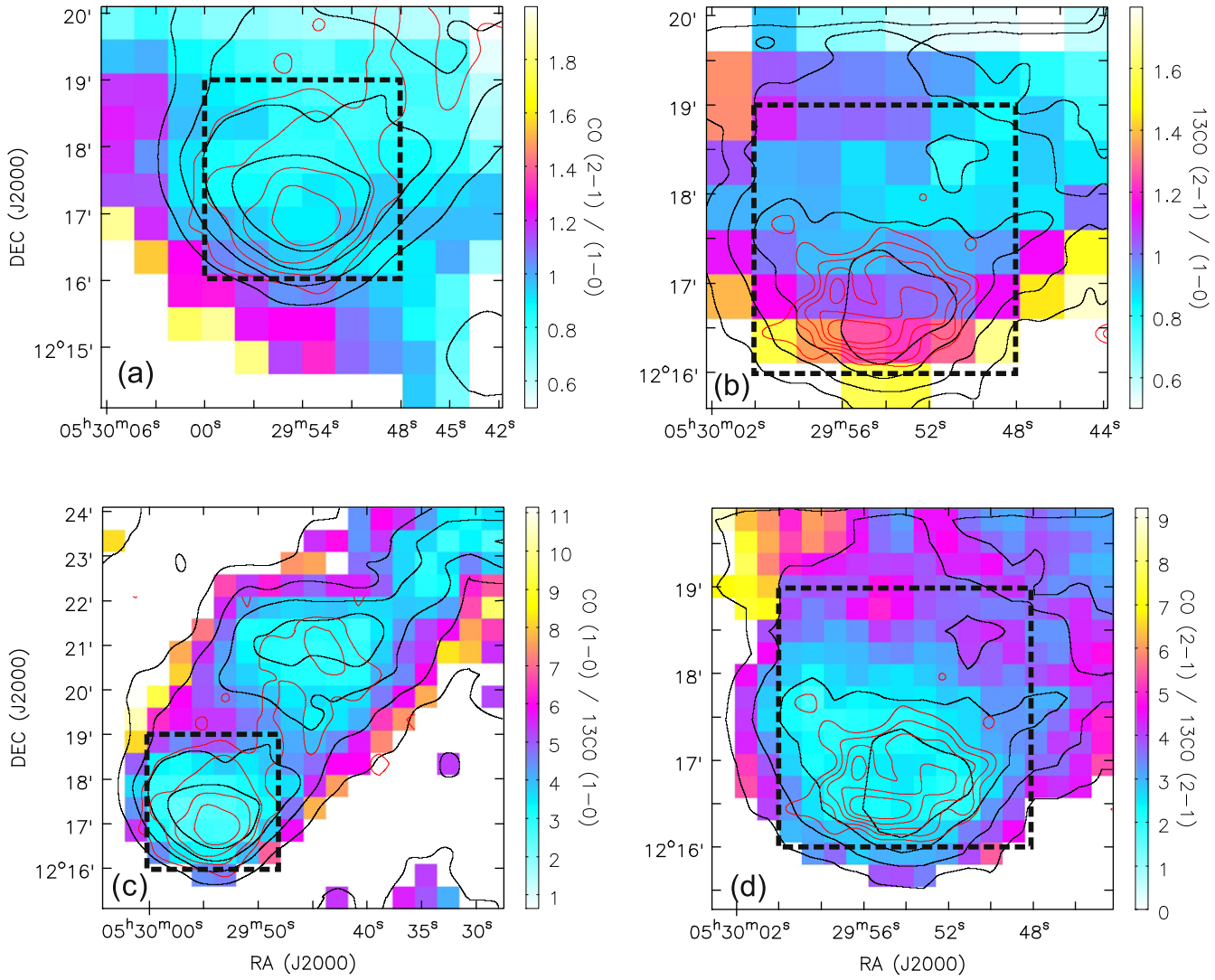

Figure 4. Integrated intensity ratios of ^{12}CO (2–1) to ^{12}CO (1–0), ^{13}CO (2–1) to ^{13}CO (1–0), ^{12}CO (1–0) to ^{13}CO (1–0), and ^{12}CO (2–1) to ^{12}CO (2–1) are shown in color images in panels (a), (b), (c), and (d), respectively. In panels (a) and (c), the black and red contours represent the integrated intensity of ^{13}CO (1–0) and C^{18}O (1–0), respectively. In panels (b) and (d), the black and red contours represent the integrated intensity of ^{13}CO (2–1) and C^{18}O (2–1), respectively. The contour levels for ^{13}CO (1–0), ^{13}CO (2–1), and C^{18}O (1–0) are from 20% to 80% in steps of 20% of their peak values. The peak values of ^{13}CO (1–0), ^{13}CO (2–1), and C^{18}O (1–0) are 10.8, 13.0, and 1.9 K km s^{-1}, respectively. The contour levels for C^{18}O (2–1) are from 50% to 90% in steps of 10% of the peak value 3.42 K km s^{-1}. The ratio maps are constructed from the data after imposing a cutoff of 5σ. For easier comparison, a dashed box of the same angular size marking the position and extent of "Clump-S" was drawn in each panel.

3.2. Dense Cores Traced by the JCMT/SCUBA-2 850 μm Continuum

As shown in the left panel of Figure 8, "Clump-S" fragments into two dense cores in the 850 μm continuum from JCMT/SCUBA-2 observations. The southern and northern cores are hereafter denoted as G192S and G192N, respectively. The two dense cores are located in a low-density halo with a mean flux density of ~0.12 Jy beam^{-1}. After subtracting a local background flux density of 0.12 Jy beam^{-1}, the two dense cores can be fitted with two Gaussian components, as shown in the middle panel. The two dense cores were unresolved by JCMT/SCUBA-2. Assuming that the dust emission is optically thin and the dust temperature equals the kinetic temperature (18.9 K) derived from CO isotopologues, the masses of the two cores can be obtained with the formula $M = S_\nu D^2/\kappa_\nu B_\nu(T_d)$ (Planck Collaboration et al. 2015), where S_ν is the flux of the dust emission at 850 μm, D is the distance, and $B_\nu(T_d)$ is the Planck function. Here the ratio of gas to dust is taken as 100. The dust opacity $\kappa_\nu = \kappa_0\left(\frac{\nu}{\nu_0}\right)^\beta = 0.018\,\mathrm{cm^2\,g^{-1}}$, where $\beta = 1.4$ is the dust opacity index obtained from PGCC catalog and $\kappa_0 = 0.01\,\mathrm{cm^2\,g^{-1}}$ is the dust opacity at 230 GHz derived from Ossenkopf & Henning (1994). The fluxes of G192N and G192S from two Gaussian component fits are 0.51 ± 0.04 and 0.27 ± 0.03 Jy, corresponding to masses of 0.43 ± 0.03 and 0.23 ± 0.03 $M_\odot$, respectively. We only considered flux uncertainties in estimating the mass uncertainties. However, other parameters such as dust temperature, dust opacity, and distance should also have a great effect on the mass measurement. For example, if we adopt a dust opacity index of 2, the inferred mass should be reduced by ~23%. In the right panel of Figure 8, we subtracted the two modeled Gaussian components and presented the residual as a color image. The total flux of the residual within the 10% contour of 850 μm

Table 1
Statistics of Integrated Intensities and Intensity Ratios

Transitions	Mean[a]	Std[a]	Min[a]	Max[a]
	Within 50% Contour of $C^{18}O$ (1–0)			
$CO/^{13}CO$ (1–0)	2.80	0.31	2.49	3.28
$CO/^{13}CO$ (2–1)	2.33	0.19	1.96	2.79
$C^{18}O$ (2–1)/(1–0)	1.51	0.23	1.24	1.87
CO (2–1)/(1–0)	0.91	0.04	0.85	0.96
^{13}CO (2–1)/(1–0)	1.04	0.13	0.91	1.26
$C^{18}O$ (1–0)[b]	1.39	0.27	1.10	1.88
^{13}CO (1–0)[b]	9.45	1.20	7.59	10.8
^{13}CO (2–1)[b]	10.3	1.59	7.38	13.0
$C^{18}O$ (2–1)[b]	2.25	0.61	1.18	3.42
N_{H_2}[c]	1.05×10^{22}	1.78×10^{21}	8.07×10^{21}	1.22×10^{22}
T_{ex}[c]	18.84	0.79	17.66	19.89
	Within 20% Contour of $C^{18}O$ (1–0)			
$CO/^{13}CO$ (1–0)	3.14	0.56	2.37	4.59
$CO/^{13}CO$ (2–1)	2.75	0.56	1.77	4.53
$C^{18}O$ (2–1)/(1–0)	1.79	0.52	1.00	3.30
CO (2–1)/(1–0)	0.90	0.07	0.79	1.06
^{13}CO (2–1)/(1–0)	1.04	0.21	0.77	1.56
$C^{18}O$ (1–0)	0.92	0.40	0.41	1.88
^{13}CO (1–0)	7.74	1.95	3.04	10.83
^{13}CO (2–1)	8.15	2.06	4.61	13.0
$C^{18}O$ (2–1)	1.58	0.70	0.30	3.42
	Within 20% Contour of ^{13}CO (1–0)			
$CO/^{13}CO$ (1–0)	4.14	1.40	2.37	8.14
$CO/^{13}CO$ (2–1)	3.50	1.20	1.77	10.10
CO (2–1)/(1–0)	0.90	0.08	0.77	1.14
^{13}CO (2–1)/(1–0)	1.11	0.29	0.72	2.27
^{13}CO (1–0)	6.23	2.35	1.79	10.83
^{13}CO (2–1)	6.62	2.41	1.21	13.0

Note.
[a] We get statistical results from pixel values after beam convolution.
[b] Units of K km s^{-1}.
[c] Units of K.

continuum emission is 1.36 ± 0.29 Jy, corresponding to a mass of $1.16 \pm 0.25\ M_{\odot}$. The core gas masses of G192N and G912S without subtracting local background are 0.53 ± 0.04 and $0.33 \pm 0.03\ M_{\odot}$, respectively. The corresponding beam-averaged column densities of G192N and G192S are $(1.1 \pm 0.1) \times 10^{22}$ and $(6.8 \pm 0.6) \times 10^{21}\ cm^{-2}$, respectively, which are used to calculate the abundances of molecules in each core as below. The beam-averaged column density of G192N is consistent with the column density estimated from CO isotopologues above. G192S has lower density than G192N. The total mass inferred from JCMT/SCUBA-2 850 μm continuum, including both dense cores and a low-density halo, is $1.94 \pm 0.32\ M_{\odot}$, which is roughly consistent with the mass $(3.0 \pm 2.4)\ M_{\odot}$. inferred from the *Planck* data, indicating that JCMT/SCUBA-2 traced the same cold component as that of *Planck*. The SCUBA-2 850 μm continuum band may be contaminated by the ^{12}CO (3–2) line (Drabek et al. 2012). From the RADEX calculation, we estimated that the integrated intensities of the ^{12}CO (3–2) line are ~22 and 21 K km s^{-1} for G192N and G192S, respectively. Adopting a molecular line conversion factor of 0.7 mJy $beam^{-1}$ per K km s^{-1} in the grade 3 weather band (Drabek et al. 2012), the contaminations of the ^{12}CO (3–2) line at the SCUBA-2 850 μm continuum band are 15.4 and 14.7 mJy $beam^{-1}$, corresponding to only ~3% and ~4% of the 850 μm flux for G192N and G192S, respectively. Therefore, line contamination does not greatly affect the mass calculation above.

3.3. Chemical Properties of Two Dense Cores

3.3.1. CO Depletion

Figure 9 shows the spectra of $J = 2$–1 of CO isotopologues from CSO observations. All the spectra are single-peaked. Weak wing emission can be identified in the ^{12}CO (2–1) emission. We fitted these spectra with Gaussian profiles and listed the fitted results in Table 2. The brightness temperature ratios of ^{13}CO (2–1) to $C^{18}O$ (2–1) toward G192N and G192S are 3.5 and 2.7, respectively. Assuming a terrestrial abundance ratio of 5.5 for $[^{13}CO/C^{18}O]$, the optical depths of ^{13}CO (2–1) toward G192N and G192S are ~1.3 and ~2.3, while the optical depths of $C^{18}O$ (2–1) toward G192N and G192S are <0.5.

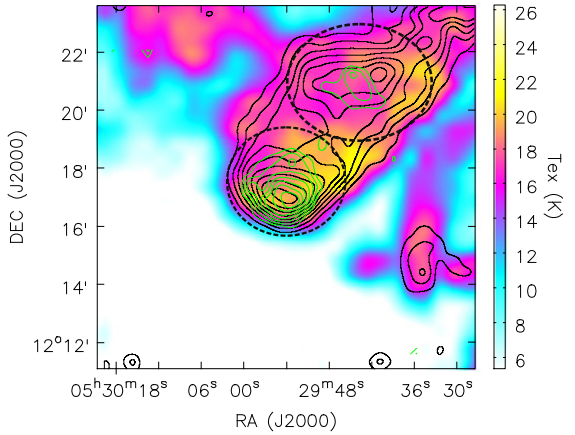

Figure 5. H_2 column density is shown in black contours. The contours are from 20% to 90% in steps of 10% of the peak value 1.22×10^{22} cm^{-2}. Integrated intensity of $C^{18}O$ (1–0) is shown in green contours. The contours are from 30% to 90% in steps of 10% of the peak value 1.88 K km s^{-1}. The excitation temperature of ^{12}CO (1–0) is shown as a color image. The two dashed ellipses mark the two gas clumps.

Compared with ^{12}CO (2–1) and ^{13}CO (2–1), $C^{18}O$ (2–1) emission is more optically thin and can reveal the actual CO column density distribution. In Figure 10, we present the integrated intensity of $C^{18}O$ (2–1) emission in blue contours and JCMT/SCUBA-2 850 μm continuum in black contours. The emission peak of $C^{18}O$ (2–1) is clearly displaced from continuum emission peaks, indicating that the CO gas may be depleted toward the clump center. Assuming LTE and optically thin for both 850 μm continuum and $C^{18}O$ (2–1) emission, the ratio of 850 μm continuum to $C^{18}O$ (2–1) could reflect the CO depletion factor in the clump neglecting any temperature change. We convolved the 850 μm data with the CSO beam and presented the flux ratio of 850 μm continuum to $C^{18}O$ (2–1) as a color image in Figure 10. The flux ratio toward the clump center is larger than the ratio at the clump edge. In the right panel of Figure 10, we investigated the circularly averaged JCMT/SCUBA-2 850 μm intensity, integrated intensity of $C^{18}O$ (2–1), and their ratio as a function of radius. JCMT/SCUBA-2 850 μm intensity drops nearly linearly from center to edge. Integrated intensity of $C^{18}O$ (2–1) peaks at $\sim$15″ from the clump center. The ratio of 850 μm intensity to integrated intensity of $C^{18}O$ (2–1) changes by a factor of five from center to edge, indicating that CO gas is severely depleted in the clump center. The column densities and abundances of $C^{18}O$ toward G192N and G192S are presented in Table 3. The $C^{18}O$ abundance of G192S is about two times larger than that of G192N, indicating that CO gas in G192N is more depleted than in G192S.

3.3.2. Molecular Abundances from KVN Observations

Figure 11 shows the spectra of N_2H^+ (1–0) toward G192N and G192S obtained with the KVN Yonsei 21 m telescope. We fitted the hyperfine structure of N_2H^+ (1–0) with the pyspeckit package[27] assuming LTE. The excitation temperature $T_{ex}(0)$, optical depth $\tau(0)$, systemic velocity $v(0)$, and velocity dispersion of the central component are shown in the upper right corners in each panel. G192N has a lower

[27] PySpecKit is an extensible spectroscopic analysis toolkit for astronomy. http://pyspeckit.bitbucket.org/html/sphinx/index.html#.

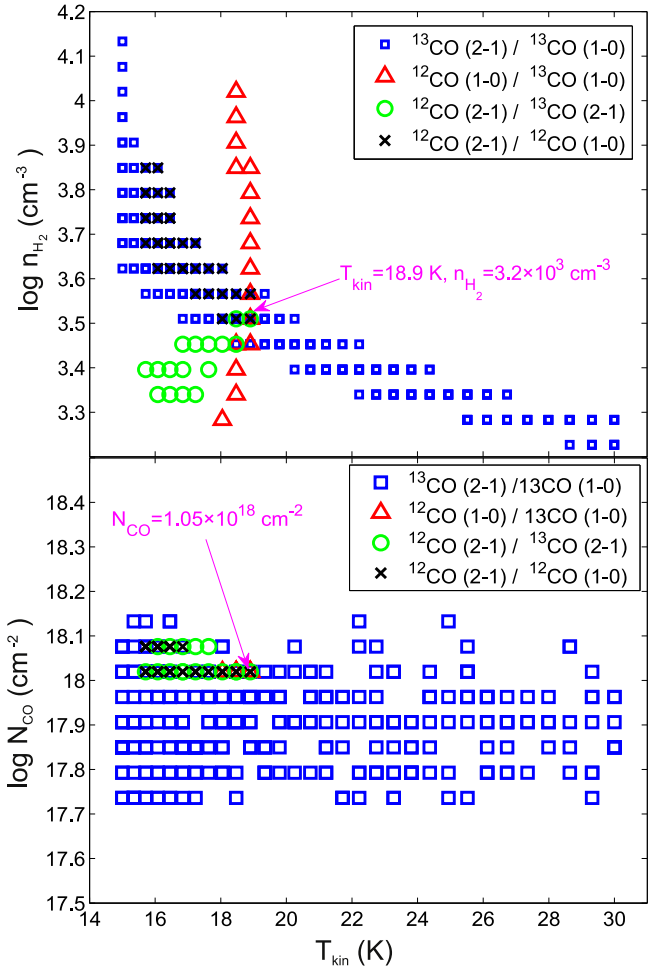

Figure 6. RADEX calculation results. Upper panel: n_{H_2} vs. T_{kin}. Lower panel: N_{CO} vs. T_{kin}. The symbols mark the parameter grids that fit the observed line ratios reasonably.

excitation temperature and a higher optical depth than G192S, indicating that G192N might be colder and denser than G192S.

Figure 12 shows spectra of other molecular transitions from the KVN single-dish observations. For G192N, both HCO^+ (1–0) and o-H_2CO ($2_{1,2} - 1_{1,1}$) lines show clear line wing emission. The o-H_2CO ($2_{1,2} - 1_{1,1}$) line has a double-peak profile and larger line width than HCO^+ (1–0), indicating that the profile of the o-H_2CO ($2_{1,2} - 1_{1,1}$) line is greatly affected by outflows. In contrast, the optically thin lines $H^{13}CO^+$ (1–0) and HDCO ($2_{0,2} - 1_{0,1}$) have much smaller line widths and seem to be unaffected by outflow activities. Interestingly, HDCO ($2_{0,2} - 1_{0,1}$) also has a double-peak profile, which might be a hint for rotation. The separation of the two peaks is $\sim$0.6 km s^{-1}, about 8 times larger than the spectral resolution (0.073 km s^{-1}). We will discuss the profile of HDCO ($2_{0,2} - 1_{0,1}$) in Section 5.2. For G192S, both HCO^+ (1–0) and o-H_2CO ($2_{1,2} - 1_{1,1}$) lines show weak line wings. $H^{13}CO^+$ (1–0) and HDCO ($2_{0,2} - 1_{0,1}$) are single-peaked and have very narrow line widths. We fitted all the spectra with Gaussian profiles and listed the results in Table 2. In general, molecular lines of G192N have larger line widths than those of G192S. The systemic velocity for both G192N and G192S is 12 km s^{-1}, which is determined from optically thin lines ($C^{18}O$ (2–1), $H^{13}CO^+$ (1–0), and HDCO ($2_{0,2} - 1_{0,1}$)).

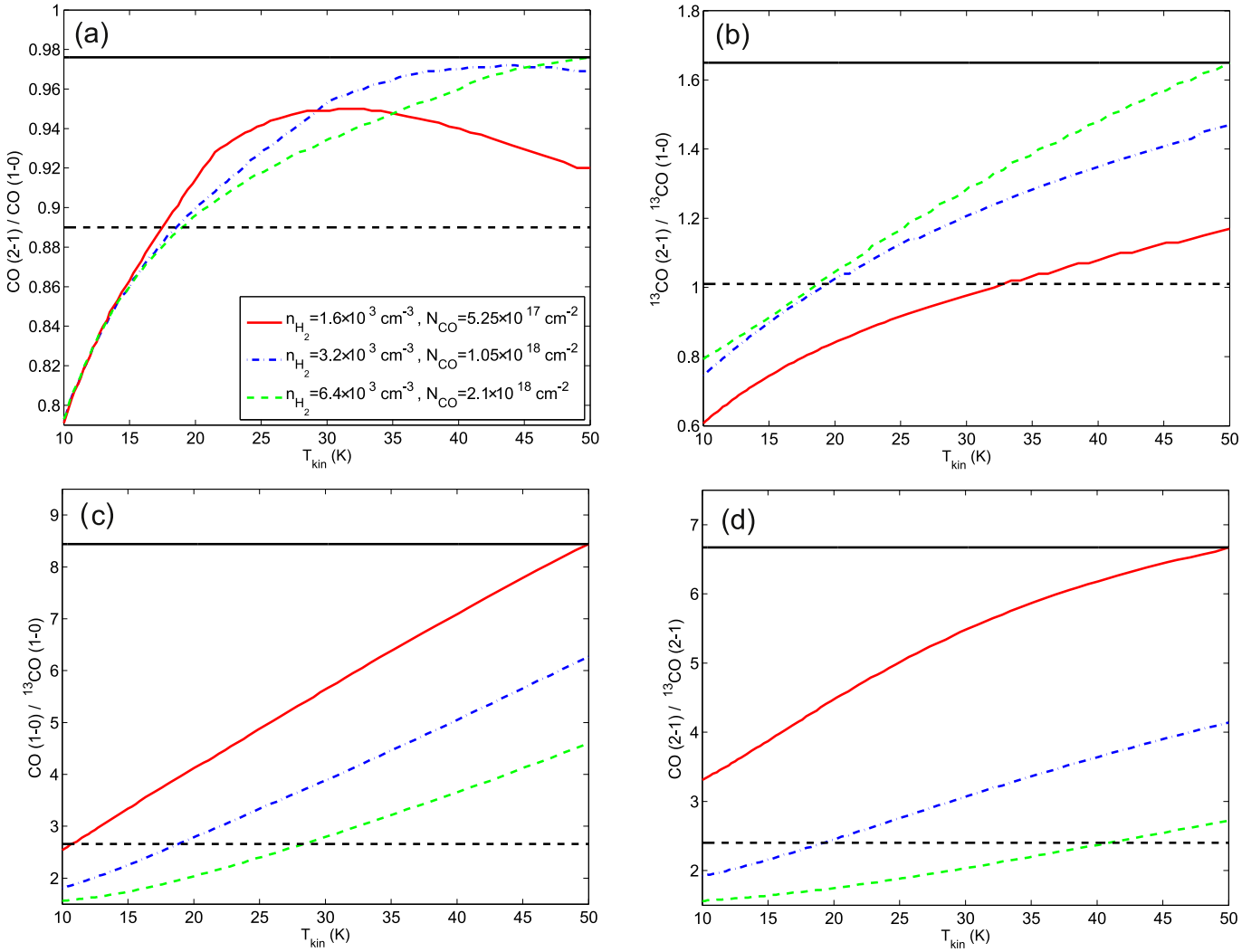

Figure 7. RADEX calculation results of intensity ratios vs. $T_{\rm kin}$. The dashed black lines represent the observed intensity ratios at core center. The solid black lines represent the maximum intensity ratios in the RADEX calculation.

For a kinetic temperature of 18.9 K, the sound speed is ~0.24 km s^{-1}. We found that the nonthermal velocity dispersions (0.33–0.39 km s^{-1}) of all optically thin lines C^{18}O (2–1), H^{13}CO$^+$ (1–0), and HDCO ($2_{0,2}$ − $1_{0,1}$) toward G192N are larger than the sound speed. The nonthermal velocity dispersions (0.28–0.31 km s^{-1}) of C^{18}O (2–1) and H^{13}CO$^+$ (1–0) toward G192S are also larger than the sound speed. The nonthermal velocity dispersion (0.20 ± 0.01 km s^{-1}) of HDCO ($2_{0,2}$ − $1_{0,1}$) toward G192S is smaller than the sound speed, indicating that the line width of HDCO ($2_{0,2}$ − $1_{0,1}$) contains a subsonic turbulent component, probably suggesting turbulence dissipation.

We calculated the beam-averaged column densities of different molecular species in Appendix B and present them in Table 3. The abundance "$X_{\rm m}$" of molecule "m" can be derived as

$$X_{\rm m} = \frac{N_{\rm m} \cdot \eta_{\rm m}}{N_{\rm H_2} \cdot \eta_{\rm c}}, \quad (1)$$

where $N_{\rm m}$, $\eta_{\rm m}$, $N_{\rm H_2}$, and $\eta_{\rm c}$ are the beam-averaged column density of molecule "m," filling factor of molecular line emission, beam-averaged column density of H_2 estimated from SCUBA-2 850 μm continuum, and filling factor of continuum emission, respectively. We remind the reader that our single-dish observations could not resolve the sources. In another Class 0 source, HH 212 located in the Orion complex, the extents of continuum and dense molecular line (e.g., HCO$^+$) emissions are about 2″–5″ (Lee et al. 2014), which are much smaller than the beam sizes of JCMT and KVN. We assume that continuum and molecular line emissions have similar source sizes that are much smaller than the beam sizes of JCMT and KVN in G192N and G192S, $\frac{\eta_{\rm m}}{\eta_{\rm c}} \approx \frac{\theta^2_{\rm KVN}}{\theta^2_{\rm JCMT}}$, where $\theta_{\rm KVN}$ and $\theta_{\rm JCMT}$ are the beam sizes of KVN and JCMT, respectively. Then the abundances were derived from Equation (1) and presented in the last column of Table 3. It should be noted that further higher angular resolution observations are needed to resolve the line and continuum emission to determine their source filling factors and to study the chemistry in detail.

G192N and G192S have a similar N_2H^+ abundance. The H^{13}CO$^+$ abundance of G192S is about 1.6 times larger than

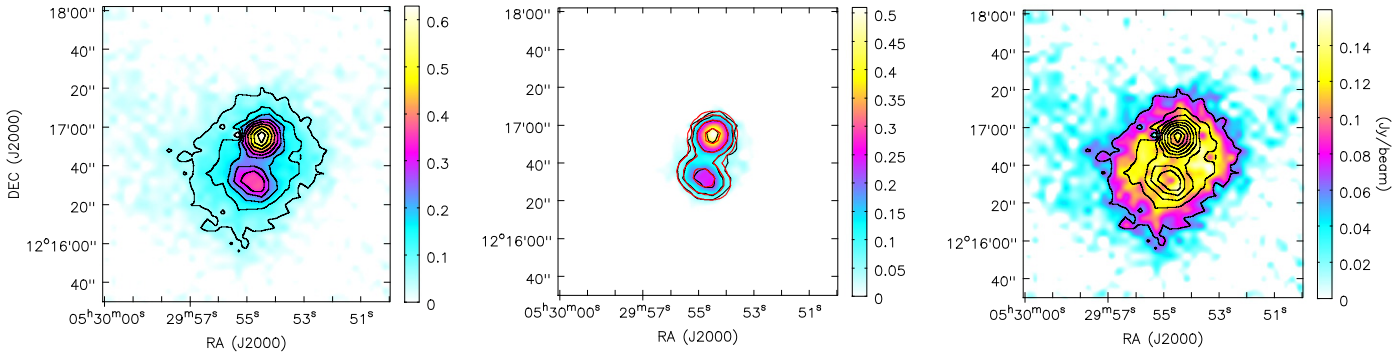

Figure 8. Left: JCMT/SCUBA-2 850 μm continuum emission is shown in contours and color scale. The contours are from 10% to 90% in steps of 10% of the peak value (0.63 Jy beam^{-1}). Middle: JCMT/SCUBA-2 850 μm continuum emission after subtracting a background value of 0.12 Jy beam^{-1} is shown in black contours and color scale. The contours are from 20% to 80% in steps of 20% of the peak value (0.51 Jy beam^{-1}). The two Gaussian components of the model emission are shown in red contours. The contours are from 20% to 80% in steps of 20% of the peak value (0.49 Jy beam^{-1}). Right: JCMT/SCUBA-2 850 μm continuum emission is shown in black contours. JCMT/SCUBA-2 850 μm continuum emission after subtracting emission of the two Gaussian components of the model emission is shown as a color image.

that of G192N, indicating that $H^{13}CO^+$ in G192N might be as depleted as CO. The HDCO column densities of G192N and G192S are $(1.9 \pm 0.1) \times 10^{12}$ and $(1.7 \pm 0.1) \times 10^{12}$ cm^{-2}, respectively. The o-H_2CO column densities of G192N and G192S are $\sim 1.5 \times 10^{14}$ and $\sim 1.1 \times 10^{14}$, respectively. Assuming that the ortho/para ratio for H_2CO is the statistical value of 3 (Roberts et al. 2002), the [HDCO]/[H_2CO] ratios of G192N and G192S are $(1.0 \pm 0.1) \times 10^{-2}$ and $(1.1 \pm 0.1) \times 10^{-2}$, respectively.

4. RESULTS OF SMA OBSERVATIONS

4.1. SMA 1.3 mm Continuum Sources and Their Associations with Infrared Sources

As shown in the left panel of Figure 13, G192N contains a compact condensation in SMA 1.3 mm continuum, which is marked with a red plus sign. Its peak position is R.A. (J2000) = 05^{h}29^{m}54^s.16 and decl. (J2000) = 12°16′53″.08. Its deconvolved FWHM angular size is 1″.26 × 0″.36 with a P.A. of 76°.3, corresponding to a radius of 255 AU at a distance of 380 pc. As marked with a blue plus sign, G192S contains a relatively weak source, which was detected at a level of 9σ. Its peak position is R.A. (J2000) = 05^{h}29^{m}54^s.35 and decl. (J2000) = 12°16′29″.68. That weak source has a deconvolved FWHM angular size of 2″.45 × 1″.43 with a P.A. of −42°.1, corresponding to a radius of 710 AU. The total fluxes of G192N and G192S in the 1.3 mm continuum are 0.223 and 0.013 Jy, respectively. The condensations detected in SMA observations are much more compact than the cold envelope traced by 850 μm continuum in JCMT/SCUBA-2 observations. The condensations G192N and G192S may be more affected by heating from protostars or outflows and should have higher dust temperatures. In Section 4.3, we will show evidence that the central region may be heated by outflows up to ∼30 K. Assuming a dust temperature of 30 K, the masses of G192N and G192S are 0.38 and 0.02 $M_\odot$, respectively. The volume densities of G192N and G192S are 7.2×10^8 and 1.9×10^6 cm^{-3}. As shown in the right panel of Figure 13, we found that the emission peaks of SMA 1.3 mm continuum for both G192N and G192S are significantly offset from the emission peaks of the JCMT/SCUBA-2 850 μm continuum. The offsets for G192N and G192S are ∼5″ and ∼7″, respectively. Such offsets are much larger than the pointing error (∼2″) of the JCMT.

As shown in the right panel of Figure 13, G192N is undetected in the *Spitzer*/IRAC 4.5 μm band. G192S shows extended 4.5 μm emission. The SMA 1.3 mm continuum emission of G192S coincides with 4.5 μm emission very well. To the west of G192S, another point source, G192SW, is seen in 4.5 μm emission but not in SMA 1.3 mm continuum emission, indicating that it might be a foreground or background star. In Figure 14, we present *Spitzer*/MIPS 70 and 24 μm emission as color images. G192N is not detected at *Spitzer*/MIPS 24 μm or IRAC bands but has a large envelope seen in *Spitzer*/MIPS 70 μm and 1.3 mm continuum from SMA observations. After subtracting a local background flux density of ∼44.9 MJy sr^{-1}, the total flux of G192N at 70 μm is 475 ± 15 mJy, corresponding to an internal luminosity of 0.21 ± 0.01 $L_\odot$ derived by using an empirical correlation between fluxes at 70 μm and internal luminosities (Dunham et al. 2008). The southern object (G192S) is a point source at *Spitzer*/MIPS 24 μm and has weak emission in *Spitzer*/MIPS 70 μm and 1.3 mm continuum. It has a flux of 184 ± 10 mJy at 70 μm, corresponding to an internal luminosity of 0.08 ± 0.01 $L_\odot$. Owing to its low luminosity, we classify it as a very low luminosity object, i.e., a VeLLo (Di Francesco et al. 2007).

It should be noted that we did not consider systematic effects (e.g., distance, calibration) on the internal luminosities. The uncertainties of internal luminosities caused by calibration uncertainties of fluxes at MIPS 70 μm are ∼20% (Evans 2007; Dunham et al. 2008). Additionally, if the distance was actually 10% higher, the internal luminosities can increase by ∼20%. Therefore, the internal luminosities estimated above have uncertainties of at least 20%.

4.2. Compact CO Outflows

Figure 15 shows the channel maps of ^{12}CO (2–1) emission from the SMA observations. The ^{12}CO (2–1) emission in the central channels [10, 14] km s^{-1} is very clumpy. Blueshifted high-velocity emission associated with G192N is clearly seen from −2 to 9 km s^{-1}, indicating that the maximum outflow velocity can be up to ∼14 km s^{-1} without correction of the inclination angle. In contrast, the redshifted high-velocity emission is much weaker, which can only be seen in channels from 15 to 17 km s^{-1}. From channel maps, one can also

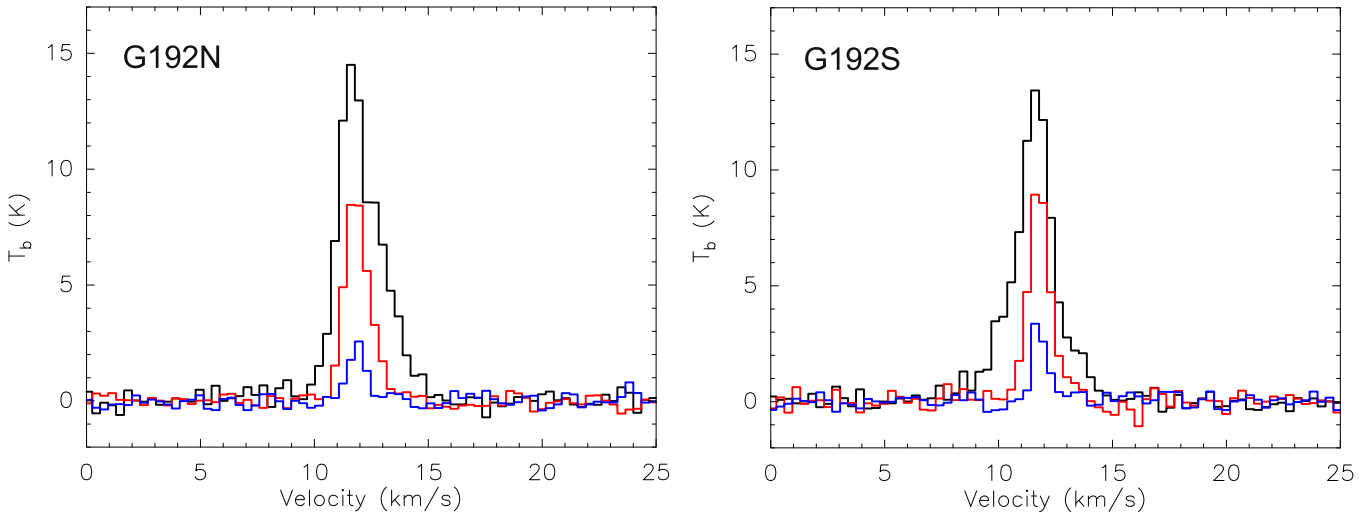

Figure 9. CSO spectra toward G192N (left) and G192S (right). Spectra of ^{12}CO (2–1), ^{13}CO (2–1), and C^{18}O (2–1) are shown in black, red, and blue, respectively.

identify weak outflows associated with G192S. The blueshifted high-velocity emission of G192S can be seen from 7 to 9 km s^{-1}, while redshifted high-velocity emission is only apparent in the 15 km s^{-1} channel. The integrated intensity of the high-velocity ^{12}CO (2–1) emission is shown in Figure 16. The outflow associated with G192N is well collimated. As shown in the right panel of Figure 16, the outflow associated with G192S is very compact and its redshifted emission and blueshifted emission overlap. We listed the radius and maximum outflow velocity of each lobe in the second and third columns of Table 4, respectively. The outflow dynamical age ($t_{\rm dyn}$) is estimated as $t_{\rm dyn} = 2R_{\rm lobe}/V_{\rm max}$ and listed in the fourth column of Table 4. $R_{\rm lobe}$ is the radius of each outflow lobe.

The gas mass of the outflow can be estimated following Qiu et al. (2009):

$$M_{\rm out} = 1.39 \times 10^{-6} \exp\left(\frac{16.59}{T_{\rm ex}}\right)(T_{\rm ex} + 0.92)D^2 \times \int \frac{\tau_{12}}{1 - e^{-\tau_{12}}} S_\nu dv, \quad (2)$$

where $M_{\rm out}$, $T_{\rm ex}$, D, τ_{12}, and S_ν are the outflow gas mass in $M_\odot$, excitation temperature of ^{12}CO (2–1), source distance in kpc, optical depth of ^{12}CO (2–1), and line flux in Jy, respectively. The mass of each outflow lobe is presented in the fifth column of Table 4. We sum both redshifted and blueshifted outflow masses to derive total outflow mass. The total outflow masses for G192N and G192S are $\sim$5.3 $\times$ 10^{-4} and $\sim$6.7 $\times$ 10^{-5} $M_\odot$, respectively.

The mass-loss rate ($\dot{M}_{\rm loss}$) of the outflow can be derived as $\dot{M}_{\rm loss} = M_{\rm out}/t_{\rm dyn}$. The total mass-loss rates of the outflows associated with G192N and G192S are 4.1 $\times$ 10^{-7} and 2.8 $\times$ 10^{-8}$M_\odot$ yr^{-1}. Under the assumption that jet energy and wind energy are due to the gravitational energy released by mass accretion onto the protostar, as stated in Bontemps et al. (1996), the outflow force ($F_{\rm out}$) is related to the mass accretion rate ($\dot{M}_{\rm acc}$) as given in the following equation obtained from the principle of momentum conservation and some manipulation of the equation:

$$\dot{M}_{\rm acc} = \frac{1}{f_{\rm ent}} \frac{\dot{M}_{\rm acc}}{\dot{M}_{\rm w}} \frac{1}{V_{\rm w}} F_{\rm flow}. \quad (3)$$

We assume a typical jet/wind velocity of $V_{\rm w} \sim 150$ km s^{-1} (Bontemps et al. 1996). $\dot{M}_{\rm w}$ is the wind/jet mass-loss rate. Models of jet/wind formation predict, on average, $\dot{M}_{\rm w}/\dot{M}_{\rm acc} \sim 0.1$ (Pelletier & Pudritz 1992; Wardle and Königl 1993; Shu et al. 1994; Bontemps et al. 1996). The entrainment efficiency is typically $f_{\rm ent} \sim 0.1-0.25$. Here we take 0.25. The outflow force F_{flow} is calculated as

$$F_{\rm flow} = \frac{P_{\rm flow}}{t_{\rm dyn}} = \frac{M_{\rm out} V_{\rm char}}{t_{\rm dyn}} = \dot{M}_{\rm out} V_{\rm char}, \quad (4)$$

where $V_{\rm char}$ is the characteristic outflow velocity, which is estimated from the intensity-weighted velocity. The calculated outflow forces and mass accretion rates are listed in the seventh and eighth columns, respectively. The total mass accretion rate for G192N is 6.3 $\times$ 10^{-7}$M_\odot$ yr^{-1}, while the total mass accretion rate for G192S is 2.8 $\times$ 10^{-8}$M_\odot$ yr^{-1}.

The accretion luminosity was calculated as

$$L_{\rm acc} = \frac{GM_{\rm acc}\dot{M}_{\rm acc}}{R}, \quad (5)$$

where $M_{\rm acc} = \dot{M}_{\rm acc} \times t_{\rm dyn}$ is the mass accreted during a dynamical time. We present the accretion luminosity in the last column of Table 4. The total accretion luminosities for G192N and G192S are 4.3 $\times$ 10^{-3} and 1.4 $\times$ 10^{-5} $L_\odot$, respectively.

In Figure 17 we present the spectra of CO lines at the emission peak of the blueshifted lobe of G192N. The PMO 13.7 m CO (1–0) and CSO CO (2–1) lines show weak line wings with $V_{\rm lsr}$ up to 8 km s^{-1} at the blueshifted side and 16 km s^{-1} at the redshifted side, respectively. However, the blueshifted high-velocity emission in SMA CO (2–1) covers a much larger velocity range from -2 to 10 km s^{-1}. For comparison, we convolved the SMA data with the CSO beam and found that even for the low-velocity part (8–10 km s^{-1}) the CSO intensity is only 3–5 times larger than the SMA emission,

Table 2
Parameters of Molecular Lines in Single-dish Observations

Lines	G192N					G192S				
	Area (K km s^{-1})	V_{lsr} (km s^{-1})	FWHM (km s^{-1})	T_b (K)	rms (K)	Area (K km s^{-1})	V_{lsr} (km s^{-1})	FWHM (km s^{-1})	T_b (K)	rms (K)
CO (2–1)	29.78 ± 0.46	11.88 ± 0.01	2.17 ± 0.04	12.86	0.33	25.99 ± 0.43	11.59 ± 0.01	2.00 ± 0.04	12.19	0.31
^{13}CO (2–1)	12.11 ± 0.24	11.84 ± 0.01	1.30 ± 0.03	8.74	0.23	11.07 ± 0.33	11.78 ± 0.01	1.13 ± 0.04	9.19	0.23
C^{18}O (2–1)	2.43 ± 0.20	11.88 ± 0.03	0.90 ± 0.09	2.53	0.23	2.72 ± 0.18	11.77 ± 0.02	0.74 ± 0.06	3.43	0.22
HCO^+ (1–0)	7.15 ± 0.04	12.48 ± 0.00	1.79 ± 0.01	3.75	0.07	5.95 ± 0.04	12.25 ± 0.01	1.37 ± 0.01	4.06	0.07
$H^{13}CO^+$ (1–0)	1.05 ± 0.03	12.08 ± 0.01	0.80 ± 0.03	1.23	0.08	1.07 ± 0.02	12.10 ± 0.01	0.68 ± 0.02	1.47	0.09
H_2CO ($2_{1,2} - 1_{1,1}$)	5.05 ± 0.05	12.50 ± 0.01	2.73 ± 0.03	1.73	0.09	3.46 ± 0.04	12.27 ± 0.01	1.60 ± 0.02	2.02	0.08
HDCO ($2_{0,2} - 1_{0,1}$)	0.59 ± 0.03	12.04 ± 0.02	0.94 ± 0.05	0.59	0.08	0.51 ± 0.02	12.15 ± 0.01	0.50 ± 0.03	0.96	0.09

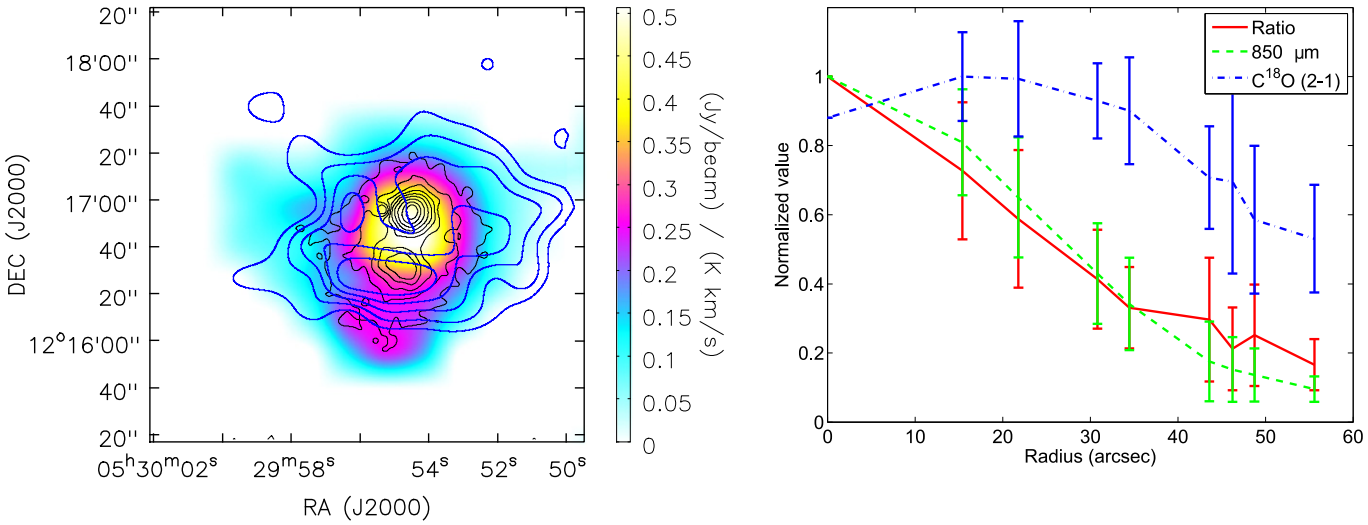

Figure 10. Left: the ratio of JCMT/SCUBA-2 850 μm intensity to integrated intensity of $C^{18}O$ (2–1) is shown as a color image. JCMT/SCUBA-2 850 μm continuum emission is shown in black contours. The contours are from 10% to 90% in steps of 10% of the peak value (0.63 Jy beam^{-1}). The blue contours represent integrated intensity of $C^{18}O$ (2–1). The contour levels are from 50% to 90% in steps of 10% of the peak value. Right: circularly averaged JCMT/SCUBA-2 850 μm intensity (after convolved with CSO beam), integrated intensity of $C^{18}O$ (2–1), and their ratio as a function of radius centered at the emission peak of 850 μm continuum emission.

Table 3
Column Densities and Abundances

Species	Column density (cm^{-2})	Abundance[a]
	G192N	
H_2[b]	$(1.1 \pm 0.1) \times 10^{22}$	...
$C^{18}O$	$(2.5 \pm 0.2) \times 10^{15}$	$(1.4 \pm 0.2) \times 10^{-6}$
$H^{13}CO^+$	$(1.1 \pm 0.1) \times 10^{12}$	$(5.2 \pm 0.5) \times 10^{-10}$
N_2H^+	$(4.4 \pm 0.6) \times 10^{13}$	$(2.1 \pm 0.4) \times 10^{-8}$
o-H_2CO	$\sim 1.5 \times 10^{14}$	$(4.1 \pm 0.3) \times 10^{-8}$
HDCO	$(1.9 \pm 0.1) \times 10^{12}$	$(5.0 \pm 0.6) \times 10^{-10}$
	G192S	
H_2[b]	$(6.8 \pm 0.2) \times 10^{21}$	...
$C^{18}O$	$(2.8 \pm 0.2) \times 10^{15}$	$(2.4 \pm 0.2) \times 10^{-6}$
$H^{13}CO^+$	$(1.1 \pm 0.1) \times 10^{12}$	$(8.4 \pm 1.0) \times 10^{-10}$
N_2H^+	$(2.3 \pm 0.5) \times 10^{13}$	$(1.8 \pm 0.4) \times 10^{-8}$
o-H_2CO	$\sim 1.1 \times 10^{14}$	$(2.9 \pm 0.3) \times 10^{-8}$
HDCO	$(1.7 \pm 0.1) \times 10^{12}$	$(7.3 \pm 0.5) \times 10^{-10}$

Notes.
[a] Corrected with the filling factor as described in Section 3.3.2.
[b] Derived from SCUBA-2 850 μm continuum as described in Section 3.2.

while the blueshifted emission in SMA CO (2–1) is mainly dominated by higher-velocity ($V_{lsr} < 8$ km s^{-1}) gas. The SMA +CSO CO (2–1) emission recovers most of the missing flux at low velocities. However, the high-velocity outflow emission is not clearly seen in either CSO or SMA+CSO CO (2–1) emission, indicating that the outflow is very compact and its emission is totally diluted by single-dish observations. Therefore, it seems that the missing flux of the SMA is not significant for high-velocity outflow gas. The outflow mass or mass-loss rate should only be underestimated by a factor of <3–5 as a result of missing flux.

4.3. Gas Fragmentation

The integrated intensity maps of SMA+CSO ^{12}CO (2–1) and ^{13}CO (2–1) emissions are shown in panels (a) and (b) of Figure 18, respectively. The ^{12}CO (2–1) emission has two emission peaks, which are offset from the 1.3 mm continuum emission. The ^{13}CO gas is highly fragmented. All the ^{13}CO emission peaks are also away from the 1.3 mm continuum peaks. We derived the excitation temperature of ^{12}CO (2–1) emission from Equation (10) assuming that its emission is optically thick. The excitation temperature is shown as a color image in panel (c) of Figure 18. Assuming that ^{13}CO (2–1) emission has the same excitation temperature as ^{12}CO (2–1) emission under LTE conditions, we derived the column density of H_2 from Equation (9) by adopting typical abundance ratios $[H_2]/[^{12}CO] = 10^4$ and $[^{12}CO]/[^{13}CO] = 60$. The H_2 column density map revealed from SMA+CSO ^{13}CO (2–1) emission data is shown in panel (d) of Figure 18. We identified nine fragments from the column density map within its 50% contour, as shown in Figure 19. From Gaussian fits, their peak positions, radii (R), and peak column densities (N_{H_2}) are derived and shown in columns (2)–(4) in Table 5. Their volume densities (n_{H_2}) and masses (M_{LTE}) are calculated as $n_{H_2} = \frac{N_{H_2}}{2R}$ and $M_{LTE} = \frac{4}{3}\pi R^3 \cdot n_{H_2} \cdot m_H \cdot \mu_g$, respectively. The Jeans masses of the fragments are derived following Wang et al. (2014):

$$M_J = \frac{\pi^{5/2} c_s^3}{6\sqrt{G^3 \rho}} = 0.877 M_\odot \left(\frac{T}{10\ \mathrm{K}}\right)^{3/2} \left(\frac{n}{10^5\ \mathrm{cm}^{-3}}\right)^{-1/2}. \quad (6)$$

We use the mean excitation temperature of ^{12}CO (2–1) emission to derive the Jeans mass for each fragment. The M_{LTE} and M_J are shown in the last two columns of Table 5. We find that the gas fragments have Jeans masses significantly larger than their LTE masses, indicating that the gas fragments will not collapse but will be dispersed eventually.

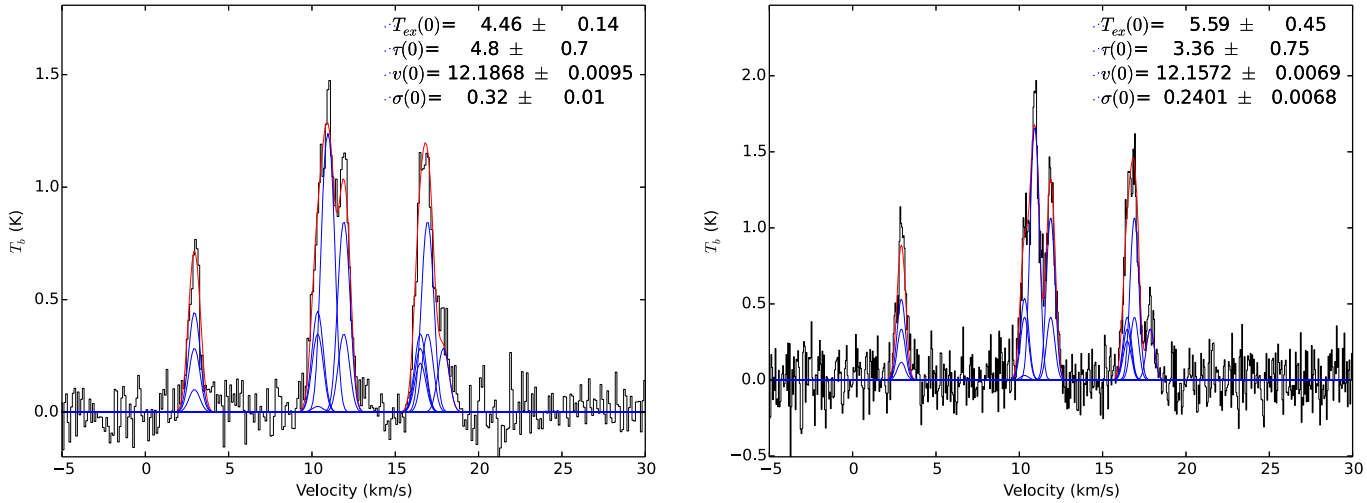

Figure 11. KVN N_2H^+ (1–0) spectra toward G192N (left) and G192S (right). The fitted hyperfine components and their sums are shown in blue and red, respectively.

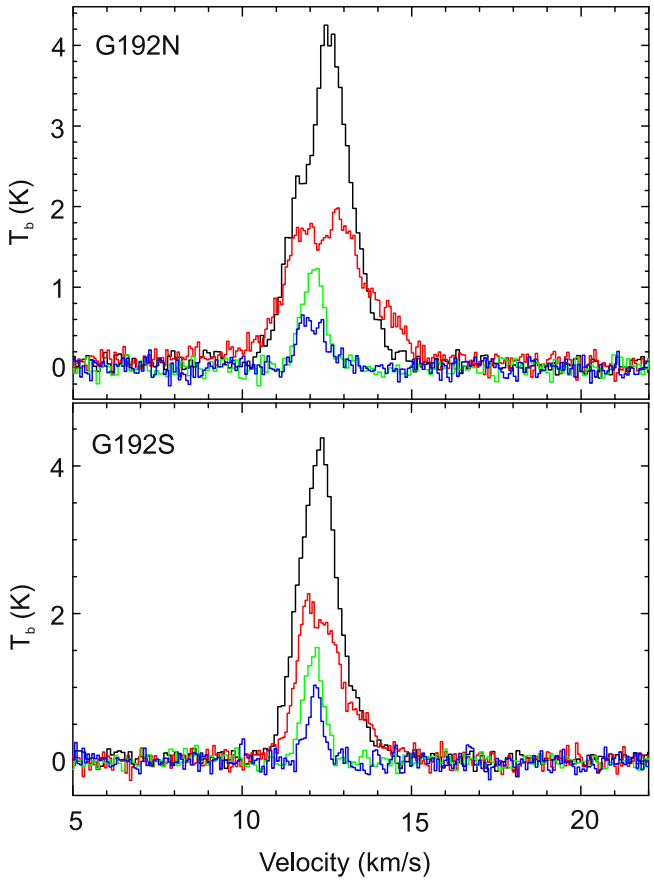

Figure 12. KVN spectra toward G192N (upper) and G192S (lower). Spectra of HCO^+ (1–0), $H^{13}CO^+$ (1–0), o-H_2CO ($2_{1,2}$ − $1_{1,1}$), and HDCO ($2_{0,2}$ − $1_{0,1}$) are shown in black, green, red, and blue, respectively.

As shown in Figure 18, the two continuum sources G192N and G192S are located in the cavities enclosed by the gas fragments, indicating that the gas distribution may be affected by ongoing star formation. In Figure 20, we plot the outflow emission contours on the excitation temperature of ^{12}CO (2–1) emission. Interestingly, we find that the CO gas at the blueshifted outflow lobe has the highest excitation temperature (∼30 K), hinting at outflow heating.

We integrated SMA ^{12}CO (2–1) emission between 10 and 14 km s^{-1} and present the integrated intensity in Figure 21. We identified eight dense and compact fragments with integrated intensity larger than 30% of the peak value 15.52 Jy beam^{-1} km s^{-1}. Figure 22 shows the beam-averaged spectra of ^{12}CO (2–1) toward each fragment. We fitted the spectra with Gaussian profiles and presented the fitted results in Table 6.

Except for G192N, the spectra of ^{12}CO (2–1) emission at other positions are all single-peaked. The SMA ^{12}CO (2–1) spectrum toward G192N shows a typical "blue profile" with the blueshifted emission peak stronger than the redshifted peak, a signature for infall motions (Zhou et al. 1993). The nondimensional parameter $\delta V = (V_{\rm thick} - V_{\rm thin})/\Delta V_{\rm thin}$ is usually used to quantify the spectral line asymmetries (Mardones et al. 1997). Here $V_{\rm thick}$ is the peak velocity of the optically thick line; $V_{\rm thin}$ and $\Delta V_{\rm thin}$ are the peak velocity and line width of the optically thin line, respectively. Infall candidates will have $\delta V < -0.25$. In the case of G192N, the δV derived from the SMA ^{12}CO (2–1) line and CSO C^{18}O (2–1) line is −3.1, much smaller than −0.25, indicating that the SMA ^{12}CO (2–1) line toward G192N might trace an infalling envelope. However, such a double-peak profile might also be caused by outflows as shown by the o-H_2CO ($2_{1,2}$ − $1_{1,1}$) line (Figure 12) or missing flux. We do not see such a double-peak profile in the SMA+CSO combined spectra because the combined data are dominated by large-scale extended emission. Higher angular resolution and higher-sensitivity observations of dense molecular tracers (e.g., HCN, HCO^+) are needed to resolve the envelope to test the infall scenario.

Fragments 1 and 3 have velocities ∼1.5 and ∼1.8 km s^{-1}, respectively, blueshifted with respect to the systemic velocity (12 km s^{-1}). Fragment 2, which is close to the blueshifted outflow lobe, is greatly affected by the outflow. The ^{12}CO (2–1) line of fragment 2 can be fitted with three Gaussian components with velocities at ∼0.2, ∼5.1, and ∼12.6 km s^{-1}, respectively. The components at ∼0.2 and ∼5.1 km s^{-1} trace outflow gas with different velocities, hinting that the outflow jet might be episodically changing. The line width of the

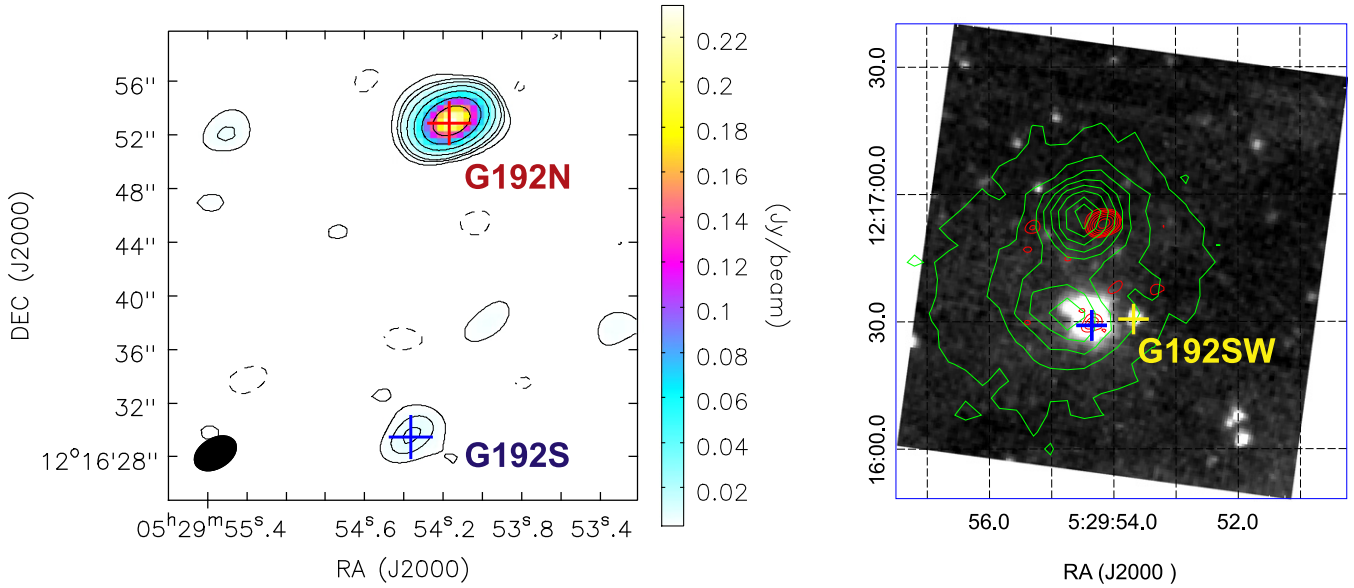

Figure 13. Left: the SMA 1.3 mm continuum is shown in black contours and color scale. The contours are $(-3, 3, 6, 9, 18, 36, 72, 144) \times 1\sigma$ ($1\sigma = 1$ mJy beam^{-1}). The red and blue plus signs mark G192N and G192S, respectively. Right: the SMA 1.3 mm continuum is shown in red contours overlayed on *Spitzer*/IRAC 4.5 μm emission. JCMT/SCUBA-2 850 μm continuum emission is shown in green contours. The contours are from 10% to 90% in steps of 10% of the peak value 0.63 Jy beam^{-1}. The yellow plus sign marks another YSO, G192SW.

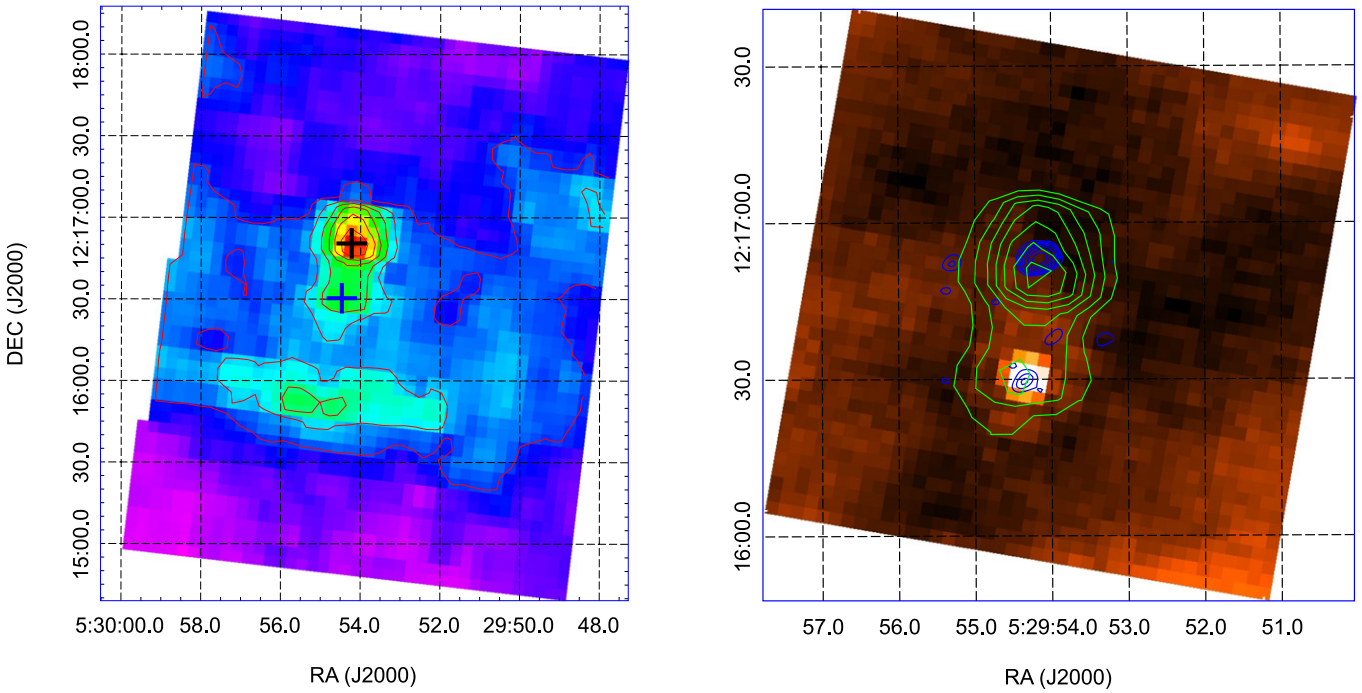

Figure 14. Left: *Spitzer*/MIPS 70 μm emission is shown in contours and color scale. The contours are from 40% to 90% in steps of 10% of the peak value 102 MJy sr^{-1}. The black and blue plus signs mark G192N and G192S, respectively. Right: *Spitzer*/MIPS 24 μm emission is shown in color scale. *Spitzer*/MIPS 70 μm emission is shown in green contours. The contours are from 50% to 95% in steps of 7.5% of the peak value 102 MJy sr^{-1}. The SMA 1.3 mm continuum is shown in blue contours. The contours are $(-3, 3, 6, 9, 18, 36, 72, 144) \times 1\sigma$ ($1\sigma = 1$ mJy beam^{-1}).

$\sim$12.6 km s^{-1} component toward fragment 2 is more than two times larger than that of fragments 1 and 3, indicating that the ^{12}CO (2–1) emission at fragment 2 may be broadened by the outflow shocks. Fragments 4, 5, and 6 are connected and located close to G192S. Fragment 6 has a velocity about 2.5 km s^{-1} redshifted to that of fragment 5, indicating that fragment 6 is impelled by the outflows. G192S itself is about 1.″6 south of fragment 5. The peak intensity of the ^{12}CO (2–1) line toward G192S is only about one-third of that of fragment 5. It seems that G192S has moved out of its natal core. Fragments 7 and 8 are located in a filament.

In conclusion, we think that the feedback of star-forming activities (e.g., outflow shocks) in this region can propel, heat, unbind, and disperse the surrounding gas.

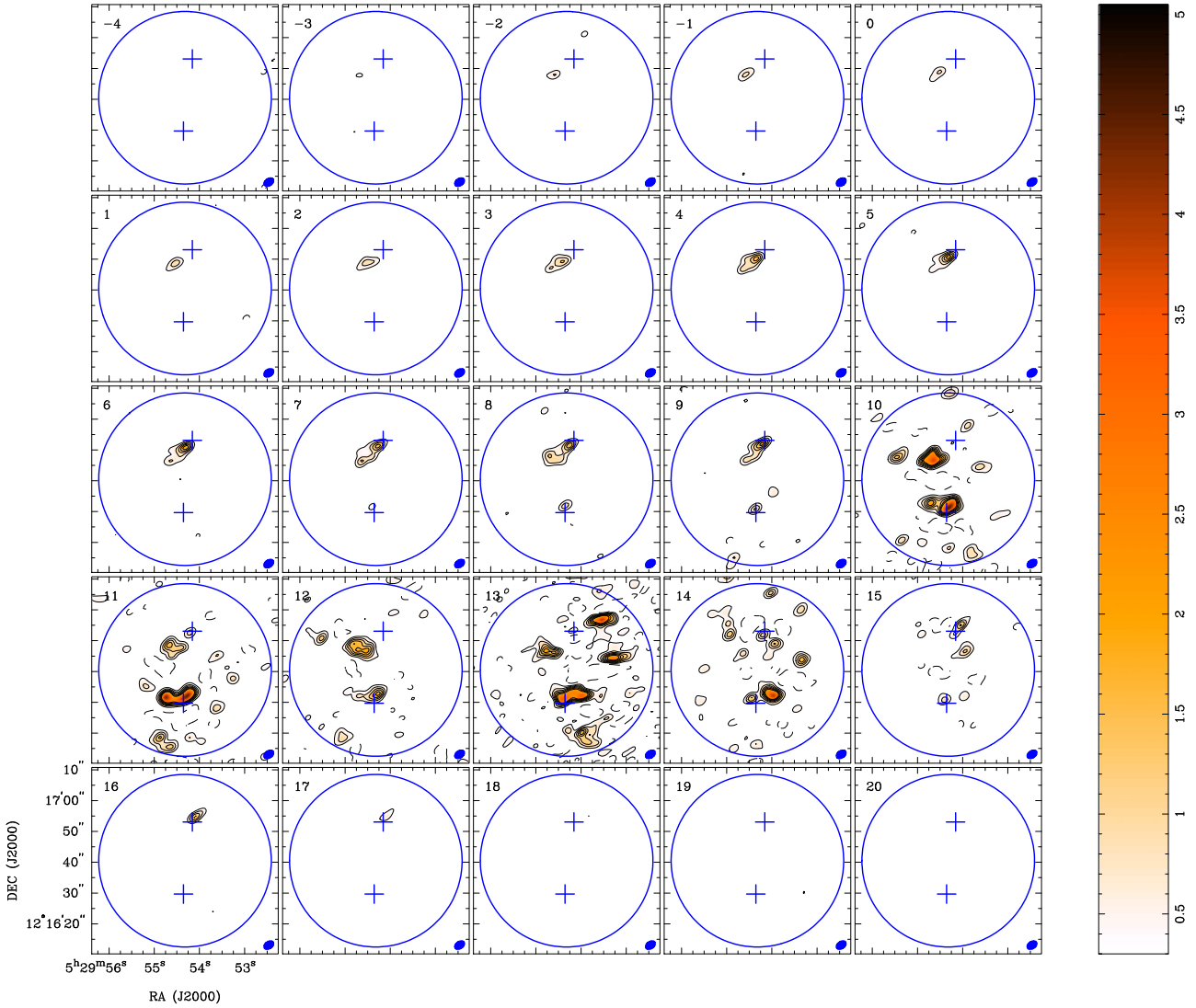

Figure 15. SMA ^{12}CO (2–1) channel map. The contours are −5 and from 5 to 30 in steps of 5σ (1σ = 0.07 Jy beam^{-1}). The primary beam of the SMA is shown in blue circles. The synthesized beam is shown as blue filled ellipses in the lower right corner of each panel. The two continuum sources G192N and G192S are marked with blue plus signs. The channel velocity is labeled in the upper left corner of each panel.

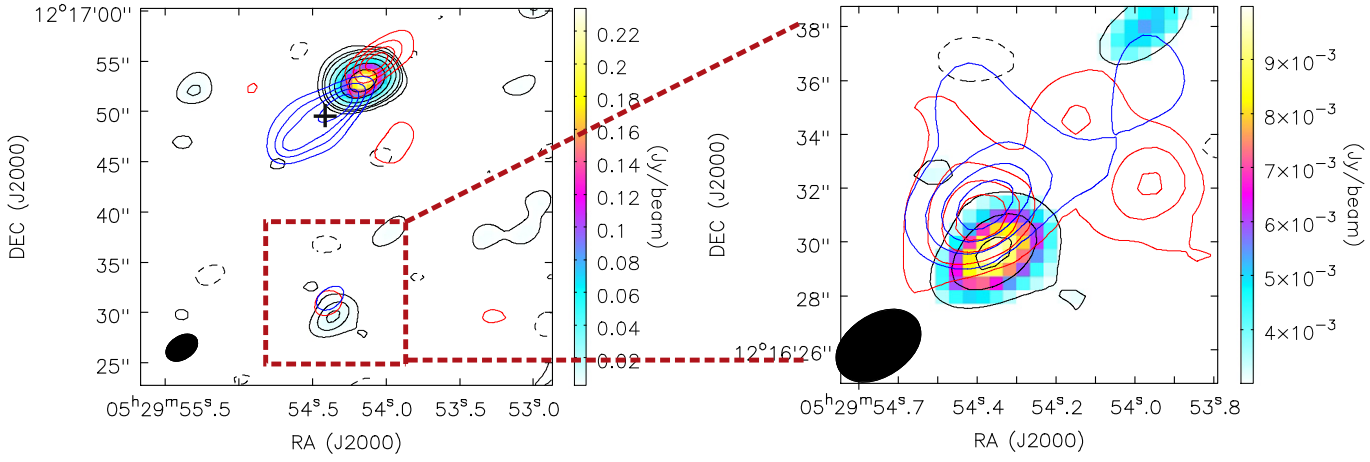

Figure 16. The SMA 1.3 mm continuum is shown in black contours and color scale. The contours are (−3, 3, 6, 9, 18, 36, 72, 144) × 1σ (1σ = 1 mJy beam^{-1}). The integrated intensities of high-velocity blueshifted (−2 to 9 km s^{-1}) and redshifted (15 to 17 km s^{-1}) ^{12}CO (2–1) emission are shown in blue and red contours, respectively. The contours for ^{12}CO (2–1) emission are from 20% to 80% of peak values. The peak values for blueshifted and redshifted emission of ^{12}CO (2–1) in the left panel are 10.82 and 3.51 Jy beam^{-1} km s^{-1}, respectively. The peak values for blueshifted and redshifted emission of ^{12}CO (2–1) in the right panel are 3.1 and 1.1 Jy beam^{-1} km s^{-1}, respectively. The emission peak of blueshifted outflow emission is marked with a black plus sign in the left panel. The spectra in Figure 17 were taken at this position.

Table 4
Parameters of CO Outflow in the SMA Observations

Lobes[a]	Radius[b] (10^3 AU)	V_{max} (km s^{-1})	Age (10^3 yr)	Mass ($10^{-5} M_\odot$)	$\dot{M}_{loss}$ ($10^{-8} M_\odot$ yr^{-1})	F_{flow} ($10^{-7} M_\odot$ km s^{-1} yr^{-1})	$\dot{M}_{acc}$ ($10^{-8} M_\odot$ yr^{-1})	L_{acc} ($10^{-5} L_\odot$)
G192N-red	0.9	5	1.7	7.4	4.5	1.8	4.8	4.0
G192N-blue	1.8	14	1.2	45	36	22	58	430
G192S-red	0.8	3	2.6	1.6	0.6	0.2	0.5	0.1
G192S-blue	1.0	4	2.3	5.1	2.2	0.9	2.3	1.3

Notes.
[a] Outflow lobes associated with G192N and G192S as shown in the left panel of Figure 16.
[b] The radius of each outflow lobe is defined as $R = \sqrt{a \cdot b}$, where a and b are the FWHM deconvolved sizes of the major and minor axes, respectively.

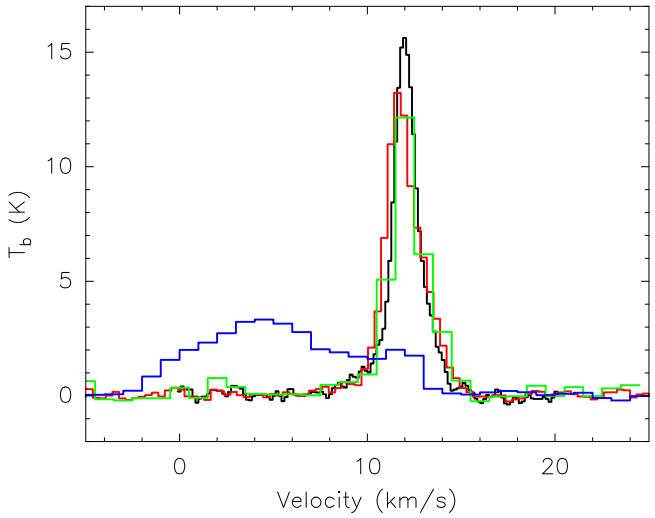

Figure 17. Spectra at the emission peak of the blueshifted outflow lobe of G192N. The beam-averaged PMO 13.7 m ^{12}CO (1–0), CSO ^{12}CO (2–1), and SMA ^{12}CO (2–1) are shown in black, red, and blue, respectively. The SMA +CSO ^{12}CO (2–1) spectrum convolved with the CSO beam is shown in green.

5. DISCUSSION

5.1. Chemical Evolutionary Stages of G192N and G192S

As shown in Table 3, the $C^{18}O$ and $H^{13}CO^+$ abundances in G192N are smaller than those in G192S, indicating that a larger amount of CO is frozen out in icy mantles, which results in a depletion of HCO^+ in G192N. As a major destroyer of N_2H^+, the absence of CO in the gas phase could enhance the abundance of N_2H^+. Indeed, the N_2H^+ abundance in G192N is larger than that in G192S. In Figure 23, we compared the N_2H^+ and $H^{13}CO^+$ abundances in G192N and G192S with that of other dense cores in the Orion A cloud (Ohashi et al. 2014). In protostellar cores, the N_2H^+ and $H^{13}CO^+$ column densities are correlated with each other (Ohashi et al. 2014). The N_2H^+ and $H^{13}CO^+$ column densities in G192S follow this correlation well. This behavior has also been observed in a large sample of IRDC clumps (Sanhueza et al. 2012), while G192N seems to have a relatively larger N_2H^+-to-$H^{13}CO^+$ abundance ratio than other protostellar cores. In warm regions, CO evaporation could destroy N_2H^+ and enhance the abundance of HCO^+ by the following reaction (Lee et al. 2004; Busquet et al. 2011):

$$N_2H^+ + CO \rightarrow HCO^+ + N_2. \quad (7)$$

The larger N_2H^+-to-$H^{13}CO^+$ abundance ratio in G192N indicates that G192N is much colder and is thus chemically younger than other protostellar cores, including G192S.

In a survey of low-mass protostellar cores, Roberts et al. (2002) found that the observed [HDCO]/[H_2CO] abundance ratios are ~0.05–0.07. These ratios are larger than those of G192N and G192S. Bell et al. (2011) found that turbulent mixing in clouds could reduce the efficiency of deuteration by increasing the ionization fraction and reducing freeze-out of heavy molecules. The low [HDCO]/[H_2CO] ratios ($\sim 1 \times 10^{-2}$) in G192N and G192S could be produced in their chemical models at very early evolutionary stages, i.e., with a chemical age less than $< 1 \times 10^4$ yr (Bell et al. 2011). As shown in the left panel of Figure 13, we notice that G192N and G192S are surrounded by extended warm dust emission as traced by 70 μm continuum. The 70 μm continuum even shows a bar-like structure close to the southern edge of the cloud, probably indicating the existence of an ionization front (IF). The IF from the H II region can heat the cloud and increase its ionization fraction, leading to lower abundances of deuterated species in prestellar phase as described in Bell et al. (2011). Therefore, we argue that the chemistry in PGCC G192.32–11.88 might be greatly affected by stellar feedback of the H II region. However, we notice that the small value of the [HDCO]/[H_2CO] ratio could also be partly attributed to the very different emission regions traced by these two isotopologues. This can be deduced from the very different line widths of the two lines (Figure 12). o-H_2CO ($2_{1,2} - 1_{1,1}$) could have a significant contribution from either outflow regions or a large volume of turbulent clouds, while HDCO ($2_{0,2} - 1_{0,1}$) may come from a compact region, which needs to be confirmed by further higher angular resolution observations in future.

Anyway, G192N and G192S are more chemically evolved than starless cores but might be still at earlier evolutionary stages than most protostellar objects so far observed.

5.2. Is G192N the Youngest Class 0 Source?

In Figure 24, we compare the infrared properties of G192N with other candidates of young Class 0 protostars (e.g., PACS Bright Red Sources [PBRSs]; Stutz et al. 2013; Tobin et al. 2015), which are deeply embedded in dense envelopes and are also either too faint ($m_{24} > 7$ mag) or undetected in the *Spitzer*/MIPS 24 μm band. Those PBRSs are very rare, and only 18 were identified in the whole Orion molecular cloud (Stutz et al. 2013). G192N is located in the same region as PBRSs in both the 70 μm flux versus 70-to-24 μm flux ratio plot and the 70-to-24 μm flux ratio versus 870-to-70 μm flux ratio plot,

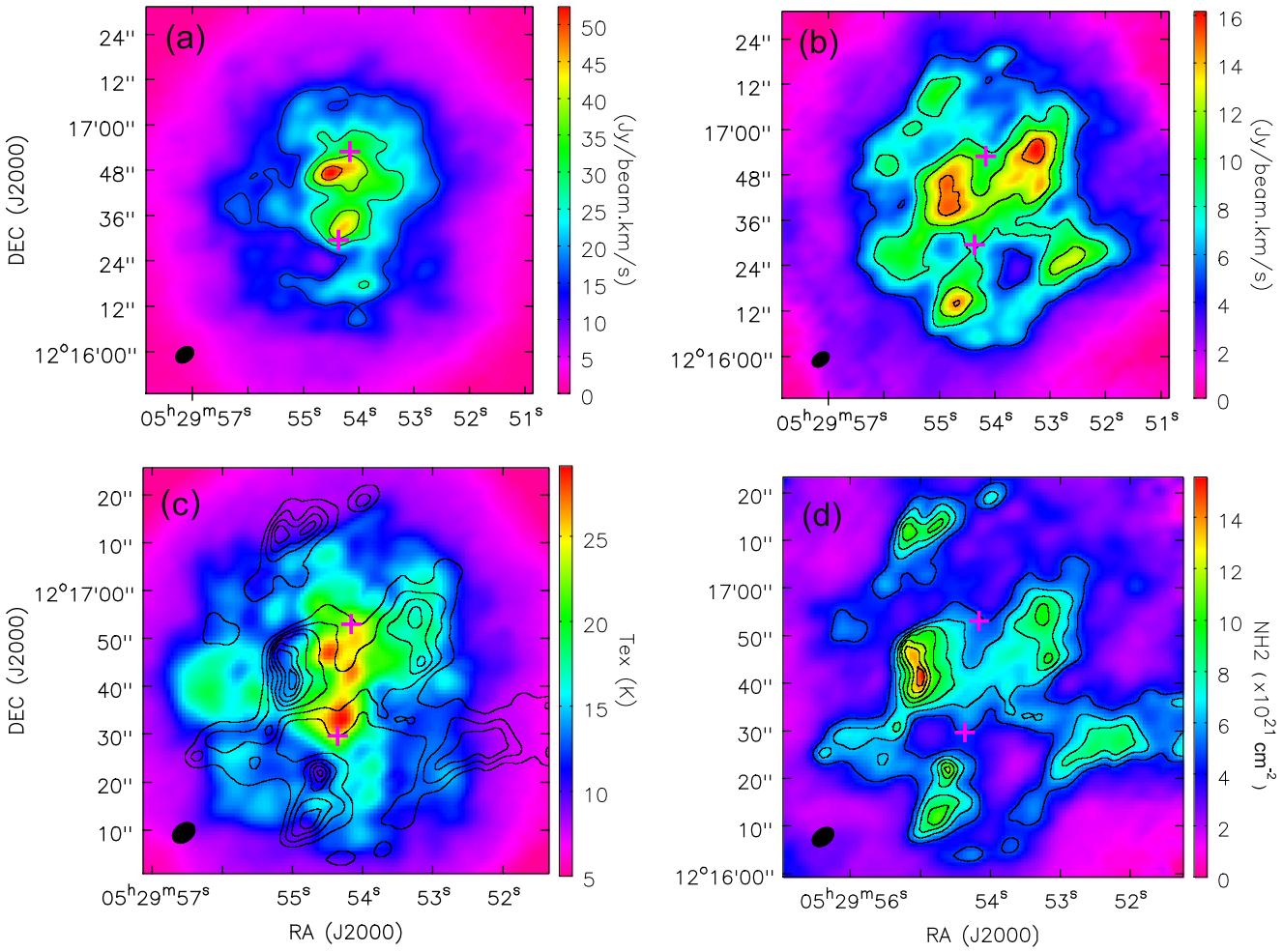

Figure 18. (a) Integrated intensity of SMA+CSO ^{12}CO (2–1) emission from 10 to 14 km s^{-1} is shown in contours overlayed on its color image. The contours are from 30% to 90% in steps of 20% of the peak value 52.5 Jy beam^{-1} km s^{-1}. (b) Integrated intensity of SMA+CSO ^{13}CO (2–1) emission from 10 to 14 km s^{-1} is shown in contours overlayed on its color image. The contours are from 30% to 90% in steps of 20% of the peak value 16.2 Jy beam^{-1} km s^{-1}. (c) H_2 column density estimated from ^{13}CO (2–1) emission is shown in contours overlayed on the color image of excitation temperature of ^{12}CO (2–1). The contours are from 30% to 90% in steps of 10% of the peak value 1.56 × 10^{22} cm^{-2}. (d) H_2 column density in contours overlayed on its color image. The two continuum sources G192N and G192S are marked with pink plus signs.

indicating that G192N should have similar properties as PBRSs. As shown in the upper panels of Figure 25, the bolometric temperature and luminosity of PBRSs in the Orion complex are strongly correlated to the flux of 70 μm emission (Stutz et al. 2013). Assuming that G192N also follows these relationships, the bolometric temperature and luminosity of G192N are derived as ~30 K and ~0.8 $L_\odot$, respectively. As shown in the lower panel of Figure 25, G192N is also located in the same region as PBRSs in the $T_{\rm bol}$ versus $L_{\rm bol}$ plot. When compared with other Class 0 protostars, PBRSs (including G192N) have relatively low bolometric temperatures. G192N itself has a relatively smaller bolometric luminosity when compared with other PBRSs.

In a survey of 15 Class 0 protostars, Yıldız et al. (2015) found that the median values of outflow mass and outflow mass-loss rate are 1.7 × 10^{-2} $M_\odot$ and 3.3 × 10^{-5}$M_\odot$ yr^{-1}, respectively, which are about two orders of magnitude larger than those values of the outflow associated with G192N. But we should note that the outflow parameters in Table 4 were not corrected with missing flux and inclination angle. As mentioned in Section 4.2, the outflow mass or mass-loss rate could be underestimated by a factor of <3–5 owing to missing flux. Since the blue and red components of the elongated outflow are well separated, neither the very low (pole-on) inclination nor the very high (edge-on) inclination is likely. The outflow mass-loss rate and accretion rate can increase by a factor of ~1.6 and 2.9, respectively, at the mean angle of 57°.3 of random outflow inclination. Even considering these effects, the outflow mass and outflow mass-loss rate of G192N are still about one order of magnitude smaller than those of other protostars. Therefore, we argue that G192S probably has the outflow with the lowest mass and mass-loss rate among known Class 0 sources.

As mentioned in Section 3.3.2, the HDCO ($2_{0,2}$ − $1_{0,1}$) line of G192N has a double-peak profile. The line width of HDCO ($2_{0,2}$ − $1_{0,1}$) is much smaller than that of the o-H_2CO ($2_{1,2}$ − $1_{1,1}$) line, indicating that its line emission is not affected by outflow activities. The critical density of HDCO ($2_{0,2}$ − $1_{0,1}$) is much larger than those of other lines (e.g., J = 1–0 of N_2H^+ and $H^{13}CO$) and therefore could trace the inner envelope or disk. Therefore, the double-peak profile of HDCO ($2_{0,2}$ − $1_{0,1}$) might be produced by rotation. If that is

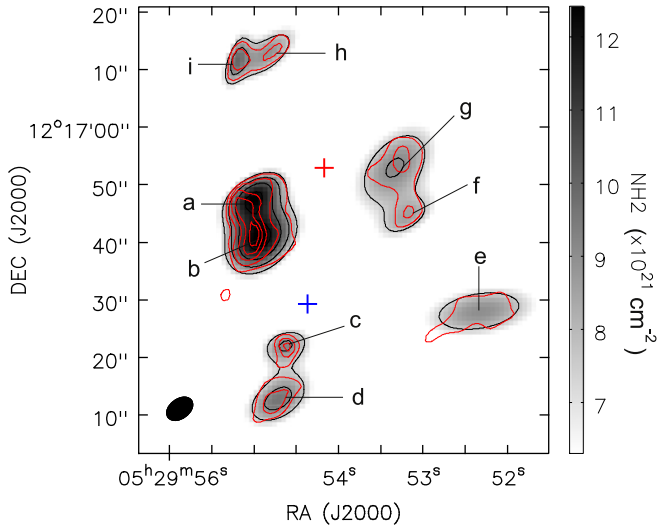

Figure 19. H_2 column density estimated from SMA+CSO ^{13}CO (2–1) emission data is shown in red contours. Gaussian fits of the nine dense fragments are shown in gray regions and black contours. The contours are from 50% to 90% in steps of 10% of the peak value 1.56×10^{22} cm^{-2}. The names of fragments are labeled from a to i. G192N and G192S are marked with red and blue plus signs, respectively.

true, we can estimate a dynamical mass $M_{\rm dyn}$ by

$$M_{\rm dyn} = \frac{R v_{\rm rot}^2}{G}, \quad (8)$$

where R is the distance to the object of mass M creating the gravitational field, G is the gravitational constant, and $v_{\rm rot}$ is the rotational velocity. Taking R of 255 AU as estimated from SMA 1.3 mm continuum and $v_{\rm rot}$ of 0.3 km s^{-1}, which is half of the velocity separation of the two emission peaks, the dynamical mass is inferred to be ~0.026 $M_\odot$, much smaller than that of other Class 0 sources (Yen et al. 2015).

In general, when compared with other young Class 0 sources in the Orion complex, G192N has potentially the smallest stellar mass and lowest bolometric luminosity and accretion rate, indicating that G192N might be at an earlier evolutionary phase than other Class 0 sources. The formation of the central protostar must be preceded by the formation of a larger, less dense, first hydrostatic core (hereafter FHSC; Larson 1969). The FHSC thus represents an intermediate evolutionary stage between the prestellar and protostellar phases. Theoretical works indicate that FHSCs might have a maximum mass of 0.01–0.1 $M_\odot$, lifetime of 0.5–50 kyr, and internal luminosity of 10^{-4}-$10^{-1} L_\odot$ (Dunham et al. 2014). Their spectral energy distributions (SEDs) are characterized by emission from 10–30 K dust and no observable emission below ~20–50 μm (Dunham et al. 2014). As mentioned before, G192N is not visible at 24 μm or shorter wavelength bands. The stellar mass (~0.026 $M_\odot$) and lifetime (1.2–1.7 kyr) estimated from outflows of G192N are consistent with the predictions of FHSCs. However, the internal luminosity (0.21 ± 0.01 $L_\odot$) of G192N is slightly larger than the upper limit of that of FHSCs. Machida et al. (2008) showed that FHSCs drive slow (~5 km s^{-1}) outflows with wide opening angles, while Price et al. (2012) showed that FHSCs can indeed produce tightly collimated outflows with speeds of ~2–7 km s^{-1}. The maximum outflow speed (>14 km s^{-1}) of G192N runs against the predictions for FHSCs. However, it should be noted that velocities >9 km s^{-1} would not be reached in the simulations of Price et al. (2012) owing to the 5 AU size of the central sink particle. When compared with other FHSC candidates (Dunham et al. 2014, and references therein), G192N is more luminous and has a more energetic outflow. Therefore, although G192N shares some similar properties to predicted FHSCs, it might be more evolved than FHSCs. G192N might be among the youngest Class 0 sources, which are slightly more evolved than an FHSC.

To summarize, we could not exclude the possibility that G192N is a relatively more evolved Class 0 object in the low-mass end of the Class 0 type distribution. Considering its low envelope mass, which is 0.35–0.43 $M_\odot$ from SMA and JCMT/SCUBA-2 observations, G192N may only form a very low mass hydrogen-burning star ($M \leqslant 0.2$ $M_\odot$) assuming a typical core-to-star formation efficiency of 30% (Alves et al. 2007; André et al. 2014). However, the dynamical age of the outflow is (1.2–1.7) $\times 10^3$ yr, which decreases to (0.8–1.1) $\times 10^3$ yr at an outflow inclination angle of 57°.3, indicating that G192N should be at a very early evolutionary phase.

5.3. Is G192S a Proto-brown Dwarf Candidate?

As shown in Figure 26, we fitted the SED of G192S with a YSO SED fitting tool (Robitaille et al. 2006, 2007). The stellar mass, disk mass, and envelope mass of the best-fit model are 0.12 $M_\odot$, 7.43 $\times 10^{-3}$ $M_\odot$, and 0.27 $M_\odot$, respectively. The envelope mass is consistent with that estimated from JCMT/SCUBA-2 850 μm continuum emission. The stellar age is 8.2×10^4 yr. The disk and envelope accretion rates are $1.5 \times 10^{-8} M_\odot$ yr^{-1} and $1.8 \times 10^{-5} M_\odot$ yr^{-1}, respectively, indicating that G192S is still at the evolutionary stage 0/I (Robitaille et al. 2006, 2007). G192S also probably has a much smaller stellar mass and envelope mass than the values estimated from SED fitting because (a) the minimum stellar mass in model SEDs of Robitaille et al. (2006, 2007) is 0.1 $M_\odot$, and thus those model SEDs could not fit stellar masses below 0.1 $M_\odot$; (b) the modeled 70 μm flux is more than 2 times larger than the observed value, indicating that the stellar mass should be overestimated; (c) as shown in the left panel of Figure 13, the 4.5 μm emission of G192S is offset from the core center in JCMT/SCUBA-2 850 μm emission, indicating that G192S might have a much smaller envelope mass than that estimated from SED modeling or JCMT/SCUBA-2 850 μm continuum emission (d). Its Vega magnitudes at *Spitzer*/IRAC 3.4 (ch1) and 4.5 (ch2) μm bands are 14.613 ± 0.009 and 12.836 ± 0.001 mag, respectively, which are compliant with the criteria (ch1-ch2 $\geqslant$ 1.5, ch2 $\leqslant$ 17.0 mag) for brown dwarf candidates (Griffith et al. 2012). Therefore, we suggest that G192S is more likely forming a brown dwarf ($M \leqslant 0.075 M_\odot$).

The accretion rate and accretion luminosity for G192S are comparable to or orders of magnitude smaller than that of other proto-brown dwarf candidates (Lee et al. 2009; Palau et al. 2014; Morata et al. 2015). For example, the typical proto-brown dwarf L328-IRS has an accretion rate and accretion luminosity of $3.6 \times 10^{-7} M_\odot$ yr^{-1} and 0.02 $L_\odot$ (Lee et al. 2009), which are about one order of magnitude larger than those of G192S. Its extremely low accretion rate ($2.8 \times 10^{-8} M_\odot$ yr^{-1}) also indicates that G192S is indeed likely to form a brown dwarf. Additionally, the 4.5 μm emission and SMA 1.3 mm continuum emission of G192S (Figure 13) are clearly offset from SCUBA-2 850 μm continuum emission and CO gas fragments, indicating that

Table 5
Parameters of ^{13}CO Fragments in the SMA+CSO Observations

Fragment	Offset[a] (arcsec, arcsec)	Radius (10^{-2} pc)	N_{H_2} (10^{21} cm^{-2})	n_{H_2} (10^4 cm^{-3})	T_{ex} (K)	M_{LTE} (10^{-1} $M_\odot$)	M_J ($M_\odot$)
a	(10.13, 8.53)	1.6	8.4	8.5	15	1.0	1.7
b	(9.08, −0.10)	2.3	12.4	8.7	17	3.1	2.1
c	(4.68, −17.82)	1.4	7.8	9.0	12	0.7	1.2
d	(5.80, −27.82)	2.2	9.6	7.1	12	2.2	1.4
e	(−29.19, −12.43)	3.2	9.0	4.6	10	4.3	1.3
f	(−17.28, 3.14)	1.5	4.9	5.3	17	0.5	2.7
g	(−14.55, 12.62)	3.3	9.2	4.5	16	4.7	2.6
h	(7.60, 32.31)	2.2	8.9	6.6	10	2.0	1.1
i	(12.96, 32.92)	<0.8	4.6	9.3	10	0.1	0.9

Note.
[a] Offset from phase center R.A. (J2000) = $05^h29^m54^s.32$ and decl. (J2000) = 12°16′40.″50.

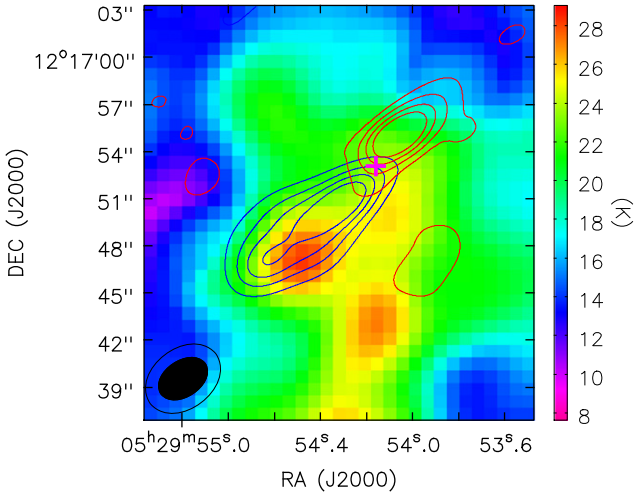

Figure 20. Integrated intensities of high-velocity blueshifted and redshifted ^{12}CO (2–1) emission are shown in blue and red contours, respectively. The contour levels are the same as in the left panel of Figure 16. The excitation temperature of ^{12}CO (2–1) is shown as the color image. G192N is marked with a pink plus sign.

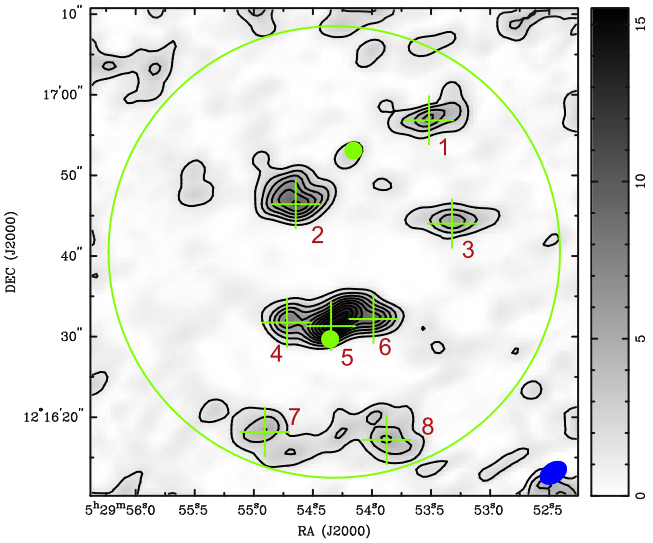

Figure 21. Integrated intensity of ^{12}CO (2–1) from 10 to 14 km s^{-1} is shown in contours. The contours are from 10% to 90% in steps of 10% of the peak value (15.52 Jy beam^{-1} km s^{-1}). The primary beam of SMA is shown by the green circle. The synthesized beam is shown by the blue filled ellipse. The two continuum sources G192N and G192S are marked with green filled circles. CO fragments with integrated intensity larger than 30% of peak value are marked with green plus signs.

G192S might have moved out of its natal envelope. The total mass estimated from SMA 1.3 mm continuum emission is only 0.02 $M_\odot$, which is insufficient for accretion to form a low-mass or very low mass star. In conclusion, we argue that G192S is an ideal proto-brown dwarf candidate.

5.4. Suppressed Star Formation in PGCC G192.32–11.88?

PGCC G192.32–11.88 is a typical bright-rimmed cloud. As shown in Figure 1, it is surrounded by Hα emission from the H II region. The *Spitzer* 70 μm continuum emission reveals hot dust inside PGCC G192.32–11.88 and possibly also traces the IF in the south. The velocity and temperature gradients revealed in line emissions of CO isotopologues also indicate that the cloud might be compressed by the H II region. All this evidence suggests that star formation in PGCC G192.32–11.88 should be affected by the feedback of the H II region.

The total mass of the dense cores G192N and G192S in Clump-S is 0.63 ± 0.06 $M_\odot$. Assuming a typical core-to-star formation efficiency of 30%, the total eventual stellar mass of Clump-S should be about 0.2 $M_\odot$. By comparing with the total clump mass (49 ± 3 or 59 ± 10 $M_\odot$) derived from CO isotopologues or virial analysis, we infer an SFE of ∼0.3%–0.4% in the southern clump of PGCC G192.32–11.88. Such a low SFE is about one order of magnitude lower than that (3%–6%) in nearby GMCs (Evans et al. 2009). We can also calculate a core formation efficiency (CFE), $M_{core}/(M_{cloud} + M_{core})$. The CFE of the southern clump in PGCC G192.32–11.88 is ∼1%. When compared with the CFE in the whole L1641 cloud, which is ∼4% and increases to the dense filaments, which is 12% (Polychroni et al. 2013), the CFE in PGCC G192.32–11.88 is much lower. It seems that star formation in PGCC G192.32–11.88 is greatly suppressed.

Additionally, as mentioned in Section 4.1, we found that G192N and G192S significantly depart from their parent cores along the direction of the velocity/temperature gradient. This offset is more evident for G192S. G192S departs about 7″ from the SCUBA-2 850 μm emission and 1.″6 from the nearest CO clump in SMA observations. It seems that G192N and G192S will move out of their parent cores, or their envelopes will be blown away owing to photo-erosion during their formation. Since G192S is close to the IF, its formation is very similar to

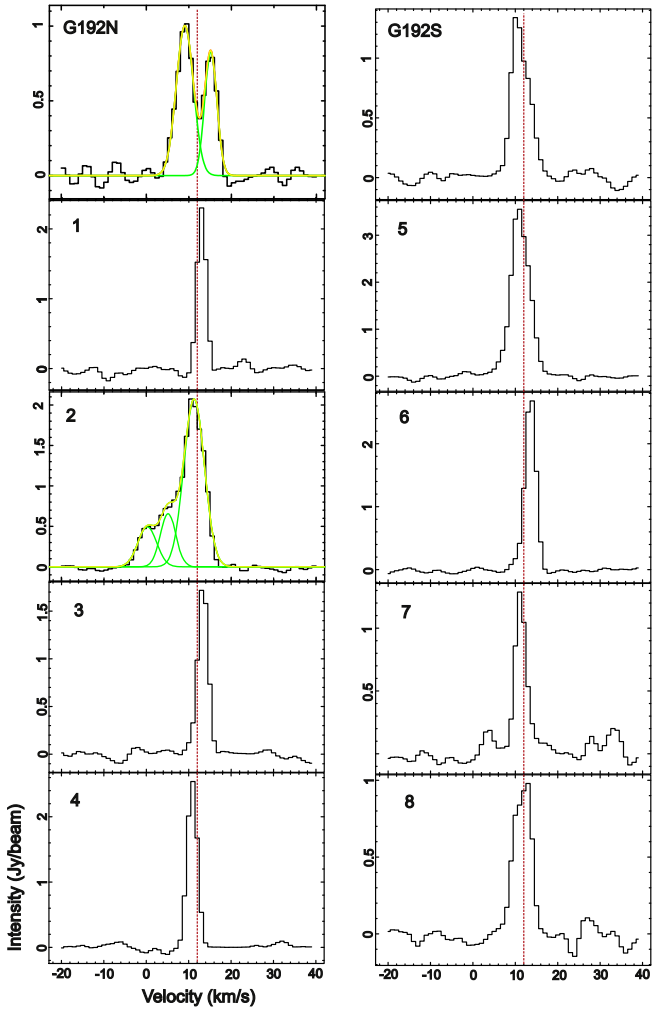

Figure 22. SMA spectra of ^{12}CO (2–1) at continuum sources and CO fragments. The vertical red lines mark the systemic velocity of 12 km s^{-1}. The green and yellow lines toward G192N and fragment 2 represent multiple Gaussian fits and their sum.

the brown dwarf formation model of Whitworth & Zinnecker (2004), in which a prestellar core's growth to a normal star is limited by photo-erosion of the ionizing radiation from a nearby OB star. We need further observations to test this scenario. Additionally, we note that a large population of brown dwarfs has been discovered in the λ Orionis complex (Barrado y Navascués et al. 2004, 2007; Bouy et al. 2009; Bayo et al. 2011, 2012). Those brown dwarfs are not located at the edges of star cluster as the ejection mechanism would predict (Bayo et al. 2011), indicating that other mechanisms (like photo-erosion) may be responsible for the brown dwarf formation in the λ Orionis complex.

At any rate, the stellar feedback seems to have a very negative effect on the star formation in PGCC G192.32–11.88.

6. SUMMARY

To investigate the effect of stellar feedback on star formation, we are performing a series of observations with ground-based telescopes (PMO 13.7 m, KVN, CSO, JCMT, and SMA) toward PGCCs in the λ Orionis complex. In this work, we report the first results toward a particular source PGCC G192.32–11.88. Our main results are summarized below.

1. Mapping observations in ^{13}CO (1–0) emission reveal two clumps in PGCC G192.32–11.88. We see a clear velocity gradient of 1.6–1.8 km s^{-1} pc^{-1} across PGCC G192.32–11.88. The excitation temperature of ^{12}CO (1–0) also reveals a temperature gradient. Through LTE and non-LTE RADEX analysis of CO isotopologues, we found that PGCC G192.32–11.88 may be externally heated by the H II region. The LTE masses of the southern and northern clumps are 49 ± 3 and 99 ± 3 $M_{\odot}$, respectively. Both clumps are gravitationally bound.

2. JCMT/SCUBA-2 observations of dust continuum emission at 850 μm detected two dense cores (G192N and G192S) in "Clump-S." G192N is undetected at *Spitzer*/MIPS 24 μm or IRAC bands but has a large envelope seen in *Spitzer*/MIPS 70 μm. The southern object (G192S) is a point source at *Spitzer*/MIPS 24 μm and has weaker 70 μm emission than G192N. G192S also shows extended 4.5 μm emission. G192N with an internal luminosity of 0.21 ± 0.01 $L_{\odot}$ shares similar infrared properties to other young Class 0 sources (e.g., PBRSs). G192S is a very low luminosity object with an internal luminosity of 0.08 ± 0.01 $L_{\odot}$. The core masses of G192N and G192S derived from 850 μm continuum are 0.43 ± 0.03 and 0.23 ± 0.03 $M_{\odot}$, respectively.

3. G192N has smaller CO and HCO^+ abundances than G192S, indicating that CO and HCO^+ gas might be more depleted toward G192N. The depletion of CO enhanced the abundance of N_2H^+ in G192N. The N_2H^+-to-$H^{13}CO^+$ abundance ratio in G192N is larger than that of other protostellar cores in the Orion A cloud, as well as G192S, indicating that G192N is colder and thus chemically younger. G192N and G192S have very low [HDCO]/[H_2CO] ratios ($<2 \times 10^{-3}$), much lower than that in other protostellar cores (Roberts et al. 2002). The H II region could heat the cloud and increase its ionization fraction, leading to lower abundances of deuterated species. The chemistry in PGCC G192.32–11.88 might be greatly affected by stellar feedback (e.g., photoionizing radiation, heating) from the H II region, which needs to be tested by further chemical studies.

4. The SMA 1.3 mm continuum may be tracing the disks or inner envelopes of G192N and G192S. The masses of G192N and G192S derived from SMA 1.3 mm continuum are 0.38 and 0.02 $M_{\odot}$, respectively. The volume densities of G192N and G192S are 7.2×10^8 and 1.9×10^6 cm^{-3}, respectively. The extremely high volume density of G192N indicates that it is at a very early evolutionary stage. The 1.3 mm continuum peaks are consistent with *Spitzer* observations but significantly offset from JCMT/SCUBA-2 850 μm continuum, indicating that G192N and G192S might have moved out of their natal envelopes.

5. The ^{12}CO (2–1) emission from the SMA observations reveals a collimated outflow associated with G192N and a weak compact outflow associated with G192S. The outflows have a dynamic timescale of $\sim 1 \times 10^3$ yr. The total mass accretion rates for G192N and G192S are $6.3 \times 10^{-7} M_{\odot}$ yr^{-1} and $2.8 \times 10^{-8} M_{\odot}$ yr^{-1}, respectively.

6. The ^{13}CO (2–1) emission from the SMA+CSO combined data is highly fragmented, and the fragments have masses much smaller than their Jeans masses, indicating that the gas fragments will be dispersed. The ^{12}CO fragment close to the blueshifted outflow lobe has the largest excitation temperature

Table 6
Parameters of CO Fragments in the SMA Observations

Fragment	Offset[a] (arcsec, arcsec)	Area (Jy beam^{-1} km s^{-1})	V_{lsr} (km s^{-1})	FWHM (km s^{-1})	I_{peak} (Jy beam^{-1})	rms (mJy beam^{-1})
G192N	(−2.38, 12.58)	5.06 ± 0.17	9.07 ± 0.04	4.74 ± 0.19	1.00	42.9
	(−2.38, 12.58)	2.99 ± 0.14	15.16 ± 0.07	3.39 ± 0.17	0.83	42.9
G192S	(0.51, −10.82)	6.77 ± 0.11	11.55 ± 0.04	5.02 ± 0.09	1.26	42.1
1	(−11.76, 16.33)	6.32 ± 0.12	13.51 ± 0.02	2.52 ± 0.05	2.35	50.7
2	(4.78, 5.93)	2.74 ± 0.08	0.24 ± 0.09	5.21 ± 0.10	0.49	24.4
	(4.78, 5.93)	3.00 ± 0.01	5.14 ± 0.08	4.30 ± 0.12	0.65	24.4
	(4.78, 5.93)	12.59 ± 0.08	11.26 ± 0.02	5.70 ± 0.03	2.07	24.4
3	(−14.61, 3.52)	5.45 ± 0.05	13.84 ± 0.01	2.88 ± 0.03	1.77	39.3
4	(5.87, −8.75)	7.85 ± 0.10	11.36 ± 0.01	2.85 ± 0.04	2.58	40.8
5	(0.40, −9.19)	19.14 ± 0.10	11.61 ± 0.01	5.14 ± 0.03	3.49	46.3
6	(−4.86, −8.31)	9.16 ± 0.07	14.08 ± 0.01	3.06 ± 0.03	2.81	24.7
7	(8.61, −22.33)	4.22 ± 0.19	11.73 ± 0.06	3.15 ± 0.17	1.25	72.4
8	(−6.50, −23.31)	5.45 ± 0.17	12.23 ± 0.08	4.98 ± 0.18	1.02	50.9

Note.
[a] Offset from phase center R.A. (J2000) = 05^{h}29^{m}54^s.32 and decl. (J2000) = 12°16′40″.50.

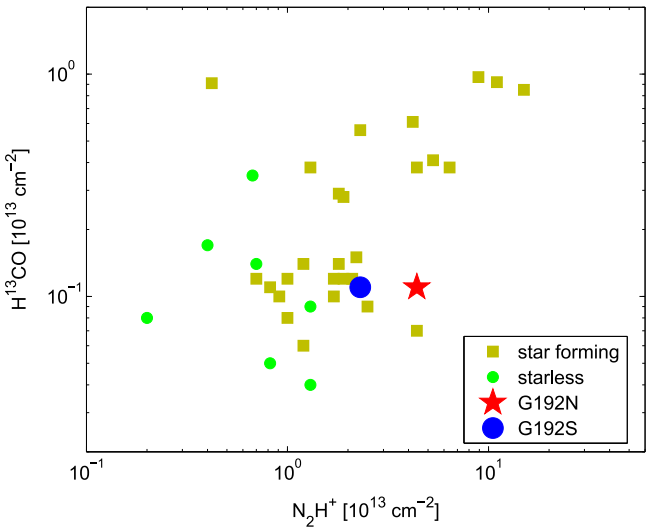

Figure 23. The column density of N_2H^+ is plotted against the column density of $H^{13}CO^+$. The data of protostellar or starless cores in the Orion A cloud are from Table 3 of Ohashi et al. (2014).

and broadened line width, hinting at outflow feedback in the form of heating and shocks.

7. G192N probably has the smallest stellar mass and lowest bolometric luminosity and accretion rate when compared with other young Class 0 sources (e.g., PBRSs), indicating that G192N might be at an earlier evolutionary phase than other Class 0 sources. G192N has slightly larger internal luminosity and outflow velocity than the predictions of first hydrostatic cores (FHSCs). Therefore, G192N might be among the youngest Class 0 sources, probably at a transitional phase from an FHSC to a Class 0 protostellar object. Considering its low internal luminosity, accretion rate, and envelope mass, G192S is an ideal proto-brown dwarf candidate. Since G192S is close to the ionization front, its formation might be greatly affected by photo-erosion of the H II region as described in the model of Whitworth & Zinnecker (2004), which needs to be confirmed by further observations.

8. The SFE (∼0.3%–0.4%) and core formation efficiency (∼1%) in PGCC G192.32–11.88 are significantly smaller than in other GMCs and dense filaments, indicating that the star formation therein is greatly suppressed owing to stellar feedback.

We are grateful to the SMA, PMO, CSO, JCMT, and the KVN staff. T.L. is supported by KASI fellowship. Y.W. is partly supported by the China Ministry of Science and Technology under State Key Development Program for Basic Research (No. 2012CB821800), the grants of NSFC No.11373009 and No.11433008. K. W. acknowledges the support from the ESO fellowship and DFG Priority Program 1573 (“Physics of the Interstellar Medium”) grant WA3628–1/1. C.W.L. was supported by the Basic Science Research Program through the National Research Foundation of Korea (NRF) funded by the Ministry of Education, Science, and Technology (NRF-2013R1A1A2A10005125) and also by the global research collaboration of the Korea Research Council of Fundamental Science & Technology (KRCF). This work was carried out in part at the Jet Propulsion Laboratory, operated for NASA by the California Institute of Technology. J.-E.L. was supported by the Basic Science Research Program through the National Research Foundation of Korea (NRF) (grant No. NRF-2015R1A2A2A01004769) and the Korea Astronomy and Space Science Institute under the R&D program (Project No. 2015–1-320–18) supervised by the Ministry of Science, ICT, and Future Planning. The KVN is a facility operated by the Korea Astronomy and Space Science Institute. S.P.L. thanks the support of the Ministry of Science and Technology of Taiwan with grant MoST 102-2119-M-007-004-MY3. Figures 24 and 25 are used with permission from Dr. A. Stutz.

APPENDIX A
LTE ANALYSIS OF $J = 1$–0 TRANSITIONS OF CO ISOTOPOLOGUES

The column density N of a linear, rigid rotor molecule can be obtained with the theory of radiation transfer and molecular

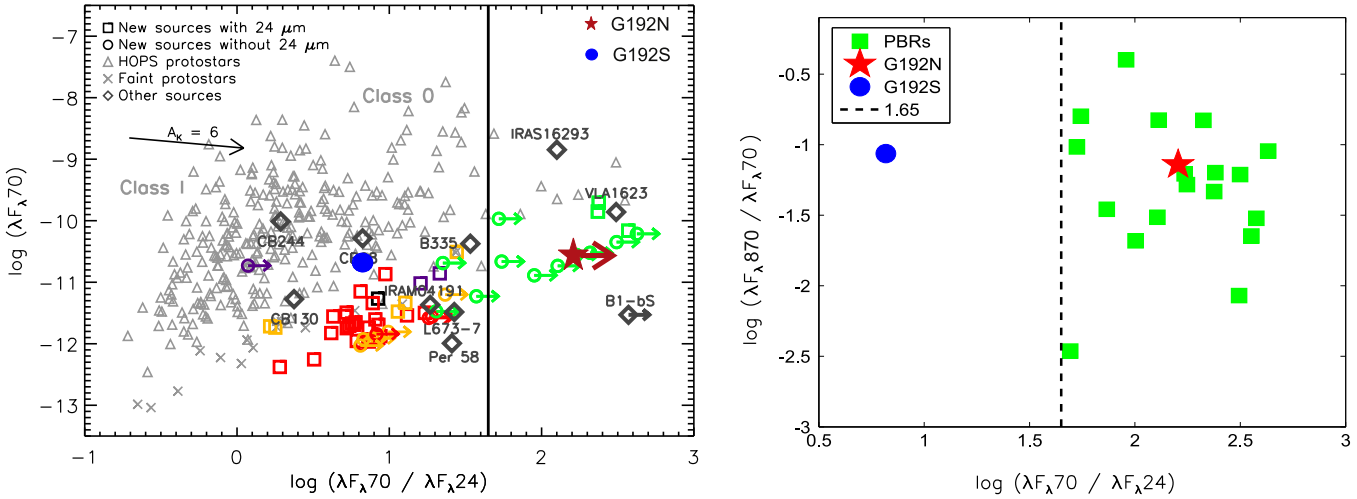

Figure 24. Left: 70 μm flux vs. 70-to-24 μm flux ratio for HOPS-detected Orion protostars (from Stutz et al. 2013). G192S and G192N are marked with a blue filled circle and a red star, respectively. Right: 70-to-24 μm flux ratio vs. 870-to-70 μm flux ratio for PBRSs. G192S and G192N are marked with a blue filled circle and a red star, respectively. The vertical lines in both panels mark the 70-to-24 μm flux ratio of 1.65, the PBRS selection criterion (Stutz et al. 2013).

excitation as follows (Garden et al. 1991):

$$N = \frac{3k}{8\pi^3 B\mu^2}\frac{\exp\left[hBJ\left(J+1\right)/kT_{\rm ex}\right]}{(J+1)} \times \frac{\left(T_{\rm ex}+hB/3k\right)}{\left[1-\exp\left(-h\nu/kT_{\rm ex}\right)\right]}\int \tau_\nu dv, \quad (9)$$

where h is the Planck constant and k is the Boltzmann constant. B, μ, J, ν, τ_ν, and $T_{\rm ex}$ are the rotational constant, permanent dipole moment, rotational quantum number of the lower state of the molecular transition, frequency, optical depth, and excitation temperature of the observed transition, respectively.

The brightness temperature of a molecular transition can be expressed as follows (Garden et al. 1991):

$$T_{\rm b} = \frac{T_{\rm a}^*}{\eta_{\rm b}} = \frac{h\nu}{k}\left[\frac{1}{\exp\left(h\nu/kT_{\rm ex}\right)-1}-\frac{1}{\exp\left(h\nu/kT_{\rm bg}\right)-1}\right] \times [1-\exp(-\tau)]f. \quad (10)$$

Here $T_{\rm a}^*$ is the antenna temperature, and $T_{\rm b}$ is the brightness temperature corrected with beam efficiency $\eta_{\rm b}$. The optical depth of ^{12}CO (1–0) can be estimated by comparing the ^{13}CO (1–0) emission with the ^{12}CO (1–0) emission (Sanhueza et al. 2012; Liu et al. 2013):

$$\frac{T_{\rm b}(^{12}{\rm CO})}{T_{\rm b}(^{13}{\rm CO})} \approx \frac{1-\exp\left(-\tau_{12}\right)}{1-\exp\left(-\tau_{13}\right)} = \frac{1-\exp\left(-\tau_{12}\right)}{1-\exp\left(-\tau_{12}/60\right)}, \quad (11)$$

where 60 is the [^{12}CO]/[^{13}CO] abundance ratio. Assuming that the ^{12}CO (1–0) emission is optically thick and that its filling factor is $f = 1$, the excitation temperature $T_{\rm ex}$ can be obtained from Equation (10).

The integral in Equation (1) can be written as (Buckle et al. 2010)

$$\int \tau(v)dv = \frac{1}{J\left(T_{\rm ex}\right)-J\left(T_{\rm bg}\right)}\int \frac{\tau(v)}{1-e^{-\tau(v)}}T_{\rm B}dv \approx \frac{1}{J\left(T_{\rm ex}\right)-J\left(T_{\rm bg}\right)}\frac{\tau(v_0)}{1-e^{-\tau(v_0)}}\int T_{\rm B}dv, \quad (12)$$

where v_0 is the central velocity of the line, $T_{\rm B}$ is the observed main-beam temperature, and $J(T)$ is the source function,

$$J(T) = \frac{T_0}{e^{T_0/T}-1}, \quad (13)$$

where $T_0 = h\nu/k_{\rm B}$, $T_{\rm bg}$ is the CMB temperature, 2.73 K.

Assuming that ^{13}CO (1–0) has the same excitation temperature as ^{12}CO (1–0), the peak optical depth $\tau(v_0)$ can be derived from Equation (10) and the column density of ^{13}CO can be calculated with Equation (9).

APPENDIX B
CALCULATION OF COLUMN DENSITY

B.1. N_2H^+

The column density of N_2H^+ is calculated as (Furuya et al. 2006)

$$N_{\rm N_2H^+} = 3.30\times10^{11}\frac{T_{\rm ex}+0.75}{1-e^{-4.47/T_{\rm ex}}}\left(\frac{\tau_{\rm tot}}{1.0}\right) \times \left(\frac{\Delta v}{1.0\ {\rm km\ s^{-1}}}\right){\rm cm^{-2}}, \quad (14)$$

where $\tau_{\rm tot}$ and Δv are the total optical depth and line width obtained from the N_2H^+ spectra through the HFS analysis.

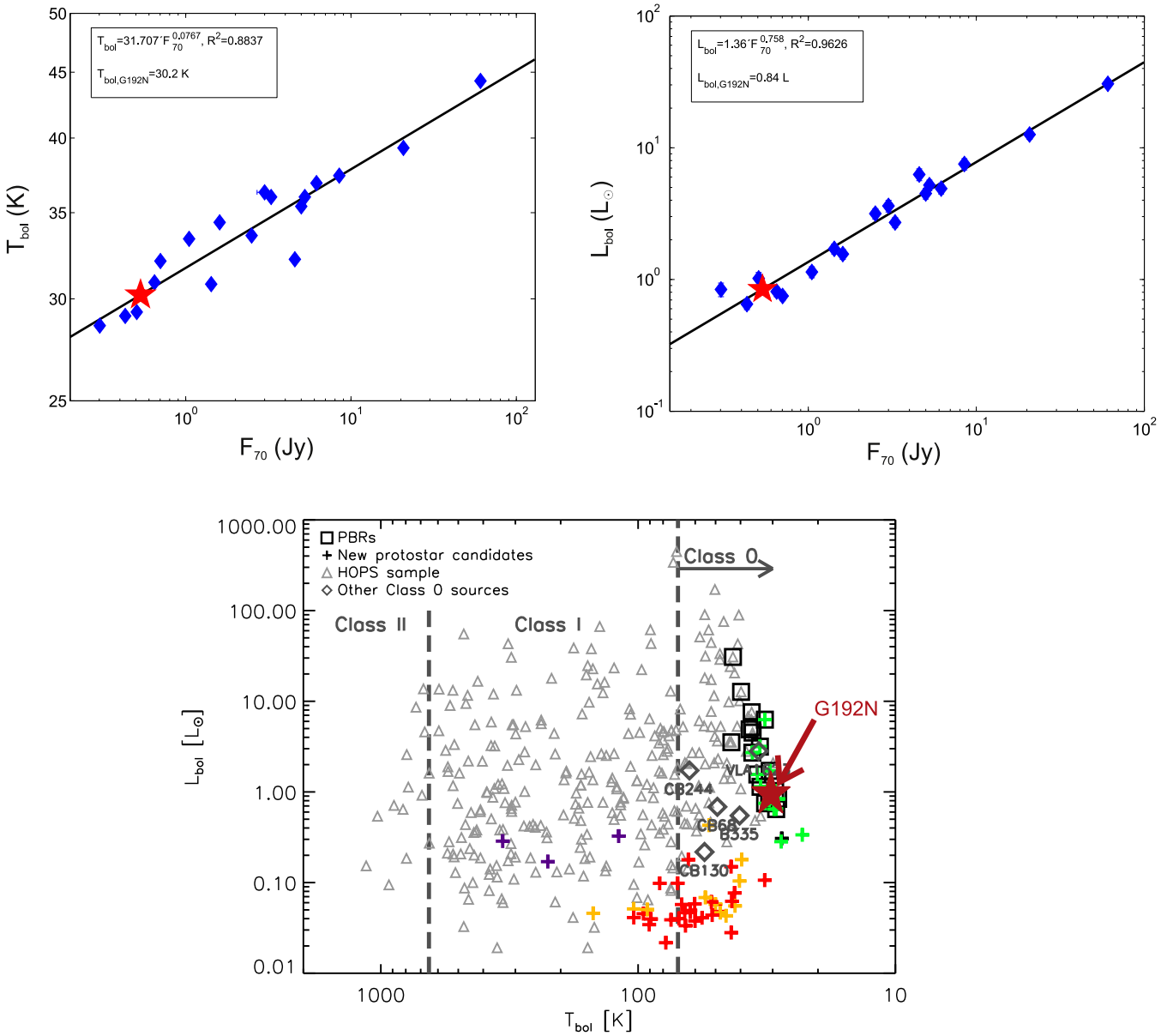

Figure 25. Upper left: 70 μm flux vs. $T_{\rm bol}$ for PBRSs. Upper right: 70 μm flux vs. $L_{\rm bol}$ for PBRSs. Lower: $T_{\rm bol}$ vs. $L_{\rm bol}$ for HOPS protostars (from Stutz et al. 2013). G192N is marked with a red star.

B.2. $H^{13}CO^+$

The optical depth of HCO^+ (1–0) (τ_{12}) can be derived using Equation (11) from the intensity ratio of HCO^+ (1–0) to $H^{13}CO^+$ (1–0). After determining the optical depth of HCO^+ (1–0), its excitation temperature can be derived from Equation (10) assuming that the filling factor is 1. In Figure 27, the intensity ratio of HCO^+ (1–0) to $H^{13}CO^+$ (1–0) and excitation temperature of HCO^+ (1–0) calculated with Equations (10) and (11) are plotted as a function of optical depth of HCO^+ (1–0). It can be seen that the excitation temperature of HCO^+ (1–0) stays constant when optical depths are larger than ~10. The excitation temperatures of HCO^+ (1–0) toward G192N and G192S are 6.79 and 7.11 K, respectively. Assuming that $H^{13}CO^+$ (1–0) has the same excitation temperature as HCO^+ (1–0), the column density of $H^{13}CO^+$ can be derived from (Furuya et al. 2006)

$$N_{\rm H^{13}CO^+} = 2.32 \times 10^{11} \frac{T_{\rm ex} + 0.69}{1 - e^{-4.16/T_{\rm ex}}} \left(\frac{1}{J(T_{\rm ex}) - J(T_{\rm bg})} \right) \times \left(\frac{\int T_b dv}{1.0\ {\rm K\ km\ s^{-1}}} \right) {\rm cm^{-2}}. \quad (15)$$

B.3. o-H_2CO and HDCO

We estimated the column density of o-H_2CO with RADEX. We adopted a kinetic temperature of 18.9 K, as determined from CO isotopologues. We convolved the SCUBA-2 850 μm

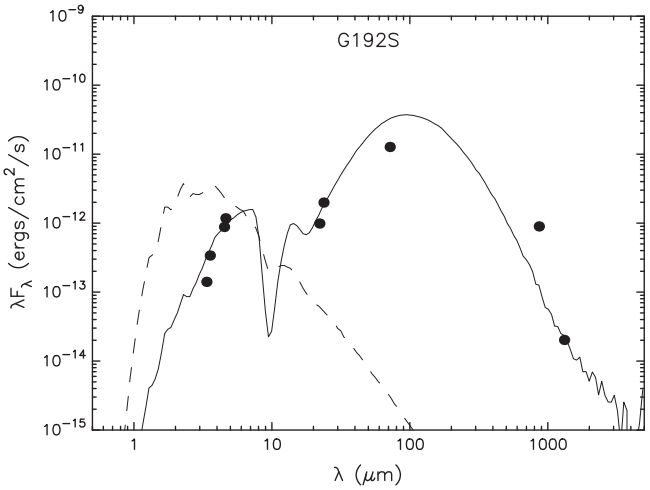

Figure 26. SED of G192S. The solid line shows the best modeled SED. The dashed line represents the best stellar fit (for comparison), including the effect of foreground extinction.

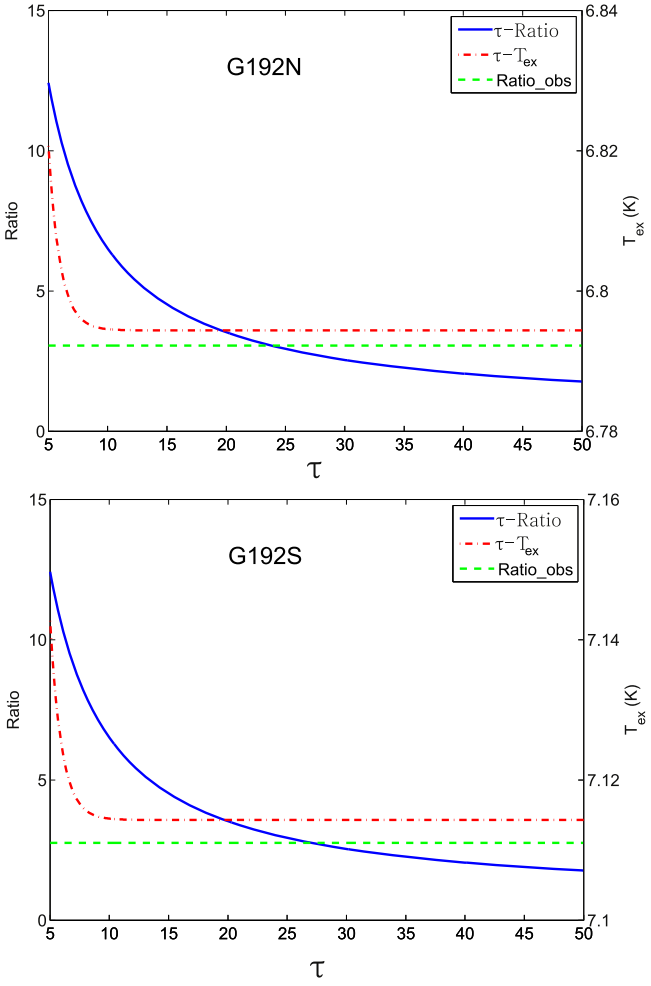

Figure 27. Intensity ratio of HCO^+ (1–0) to $H^{13}CO^+$ (1–0) and excitation temperature of HCO^+ (1–0) vs. optical depth of HCO^+ (1–0).

data with the KVN beam (24″). Then we derived a mean volume density of $2.1 \times 10^4\,\mathrm{cm}^{-3}$ from the Gaussian fit toward the continuum source. Since o-H_2CO ($2_{1,2} - 1_{1,1}$) has a much higher critical density than $J = 1$–0 and 2–1 transitions

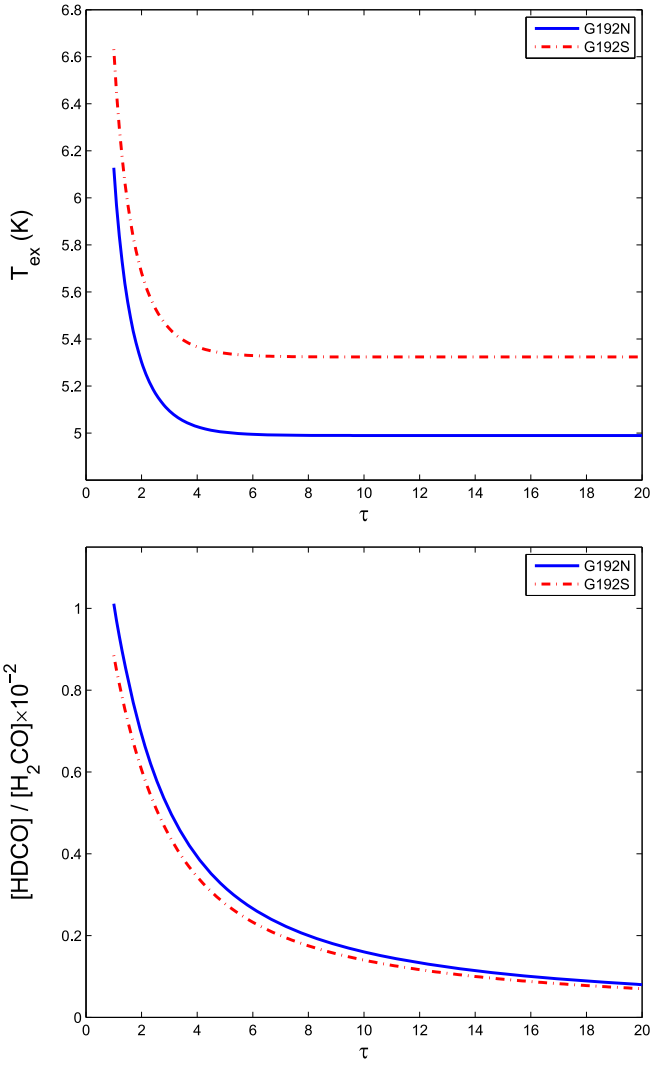

Figure 28. Excitation temperature of H_2CO ($2_{1,2} - 1_{1,1}$) (upper) and [HDCO]/[H_2CO] ratio (lower) vs. optical depth of H_2CO ($2_{1,2} - 1_{1,1}$).

of CO isotopologues (Shirley 2015), we adopt $2.1 \times 10^4\,\mathrm{cm}^{-3}$ in RADEX calculations. From RADEX calculations, we found that the column density and excitation temperature of o-H_2CO found in G192N are $\sim 1.1 \times 10^{15}\,\mathrm{cm}^{-2}$ and ~5.0 K, respectively. For G192S, the column density and excitation temperature of o-H_2CO are $\sim 7.8 \times 10^{14}\,\mathrm{cm}^{-2}$ and ~5.3 K, respectively.

Assuming that HDCO ($2_{0,2} - 1_{0,1}$) is optically thin and has the same excitation temperature as o-H_2CO ($2_{1,2} - 1_{1,1}$), the column density of HDCO can be calculated following Roberts et al. (2002):

$$N_{\mathrm{TOT}} = N_{\mathrm{u}} Q(T_{\mathrm{ex}}) e^{-E_{\mathrm{u}}/kT_{\mathrm{ex}}} / g_{\mathrm{u}}, \tag{16}$$

where N_{TOT} is the total column density, Q(Tex) is the partition fraction, and g_{u} is the degeneracy factor in the upper energy level. N_{u} is the column density in the upper level of the transition:

$$N_{\mathrm{u}} = \frac{8\pi k \nu^2}{A_{ul} hc^3} \int T_{\mathrm{b}} dv. \tag{17}$$

The HDCO column densities of G192N and G192S are $(1.9 \pm 0.1) \times 10^{12}$ and $(1.7 \pm 0.1) \times 10^{12}\,\mathrm{cm}^{-2}$, respectively. Assuming that the ortho/para ratio for H_2CO is the

statistical value of 3 (Roberts et al. 2002), the [HDCO]/[H_2CO] ratios of G192N and G192S are $(1.0 \pm 0.1) \times 10^{-2}$ and $(1.1 \pm 0.1) \times 10^{-2}$, respectively.

We can also calculate the o-H_2CO column density with Equation (16). In the optically thin case, the o-H_2CO column densities of G192N and G192S are $\sim 1.2 \times 10^{14}$ and $\sim 7.1 \times 10^{13}$ cm^{-2}, respectively. The corresponding [HDCO]/[H_2CO] ratios of G192N and G192S are $\sim 1.6 \times 10^{-2}$ and $\sim 1.4 \times 10^{-2}$, respectively, which are larger than the values obtained from RADEX calculations and should be taken as upper limits. In the optically thick case, the column density of o-H_2CO should be corrected with a factor of $\frac{\tau}{1 - e^{-\tau}}$, where τ is the optical depth of o-H_2CO ($2_{1,2} - 1_{1,1}$). The excitation temperatures of o-H_2CO ($2_{1,2} - 1_{1,1}$) toward G192N and G192S derived from RADEX calculations are consistent with the values derived by assuming LTE and that o-H_2CO ($2_{1,2} - 1_{1,1}$) emission is optically thick ($\tau > 5$), as shown in the upper panel of Figure 28. In the lower panel of Figure 28, we show the [HDCO]/[H_2CO] ratio as a function of the optical depth of o-H_2CO ($2_{1,2} - 1_{1,1}$). When compared with the value derived in the optically thin case, the [HDCO]/[H_2CO] ratio decreases by a factor of larger than five if the optical depth of o-H_2CO ($2_{1,2} - 1_{1,1}$) is larger than 6. Therefore, we argue that [HDCO]/[H_2CO] ratios of G192N and G192S might be even lower than 0.01, which needs to be confirmed by further observations.

REFERENCES

Alves, J., Lombardi, M., & Lada, C. J. 2007, A&A, 462, L17
André, P., Di Francesco, J., & Ward-Thompson, D. 2014, in Protostars and Planets VI, ed. H. Beuther et al. (Tucson, AZ: Univ. Arizona Press)
Arce, H. G., Borkin, M. A., Goodman, A. A., et al. 2011, ApJ, 742, 105
Barrado y Navascués, D., Bayo, A., Morales-Calderón, M. ., et al. 2007, A&A, 468, L5
Barrado y Navascués, D., Stauffer, J. R., & Bouvier, J. 2004, ApJ, 610, 1064
Bayo, A., Barrado, D., & Huélamo, N. 2012, A&A, 547, 80
Bayo, A., Barrado, D., Stauffer, J., et al. 2011, A&A, 536, 63
Bell, T. A., Willacy, K., Phillips, T. G., et al. 2011, ApJ, 731, 48
Bertoldi, F., & McKee, C. F. 1990, ApJ, 354, 529
Bontemps, S., André, P., Terebey, S., & Cabrit, S. 1996, A&A, 311, 858
Bouy, H., Huélamo, N., Barrado Y Navascués, D., et al. 2009, A&A, 504, 199
Brand, J., Massi, F., Zavagno, A., et al. 2011, A&A, 527, 62
Buckle, J. V., Curtis, E. I., Roberts, J. F., et al. 2010, MNRAS, 401, 204
Busquet, G., Estalella, R., Zhang, Q., et al. 2011, A&A, 525, 141
Chen, W. P., Lee, H. T., & Sanchawala, K. 2007, IAUS, 237, 278
Cunha, K., & Smith, V. V. 1996, A&A, 309, 892
Dale, J. E., Ercolano, B., & Bonnell, I. A. 2012, MNRAS, 427, 2852
Dale, J. E., Ercolano, B., & Bonnell, I. A. 2013, MNRAS, 431, 1062
Dale, J. E., Haworth, T. J., & Bressert, E. 2015, MNRAS, 450, 1199
Deharveng, L., Lefloch, B., Kurtz, S., et al. 2008, A&A, 482, 585
Deharveng, L., Lefloch, B., Zavagno, A., et al. 2003, A&A, 408, L25
Deharveng, L., Zavagno, A., & Caplan, J. 2005, A&A, 433, 565
Di Francesco, J., Evans, N. J., II, Caselli, P., et al. 2007, in Protostars and Planets V, ed. B. Reipurth, D. Jewitt, & K. Keil (Tucson, AZ: Univ. Arizona Press), 17
Dolan, C. J., & Mathieu, R. D. 2001, AJ, 121, 2124
Dolan, C. J., & Mathieu, R. D. 2002, AJ, 123, 387
Drabek, E., Hatchell, J., Friberg, P., et al. 2012, MNRAS, 426, 23
Dunham, M. M., Crapsi, A., Evans, N. J., II, et al. 2008, ApJ, 179, 249
Dunham, M. M., Stutz, A. M., Allen, L. E., et al. 2014, in Protostars and Planets VI, ed. H. Beuther et al. (Tucson, AZ: Univ. Arizona Press)
Evans, N. J., II, et al. 2007, Final Delivery of Data from the c2d Legacy Project: IRAC and MIPS (Pasadena, CA: SSC) http://ssc.spitzer.caltech.edu/legacy/all.html
Evans, N. J., II, Dunham, M. M., Jorgensen, J. K., et al. 2009, ApJS, 181, 321
Elmegreen, B. G., & Lada, C. J. 1977, ApJ, 214, 725
Furuya, R. S., Kitamura, Y., & Shinnaga, H. 2006, ApJ, 653, 1369
Garden, R. P., Hayashi, M., Hasegawa, T., Gatley, I., & Kaifu, N. 1991, ApJ, 374, 540
Griffith, R. L., Kirkpatrick, J. D., Eisenhardt, P. R. M., et al. 2012, AJ, 144, 148
Guilloteau, S., & Lucas, R. 2000, in ASP Conf. Ser. 217, Imaging at Radio through Submillimeter Wavelengths, ed. J. G. Mangum, & S. J. E. Radford (San Francisco, CA: ASP), 299
Ho, P. T. P., Moran, J. M., & Lo, K. Y. 2004, ApJL, 616, L1
Juvela, M., Ristorcelli, I., Pagani, L., et al. 2012, A&A, 541, 12
Kim, K.-T., Byun, D.-Y., Je, D.-H., et al. 2011, JKAS, 44, 81
Krumholz, M. R., Bate, M. R., Arce, H. G., et al. 2014, in Protostars and Planets VI, ed. H. Beuther et al. (Tucson, AZ: Univ. Arizona Press)
Larson, R. B. 1969, MNRAS, 145, 271
Lee, C.-F., Hirano, N., Zhang, Q., et al. 2014, ApJ, 786, 114
Lee, C. W., Bourke, T. L., Myers, P. C., et al. 2009, ApJ, 693, 1290
Lee, H.-T., Chen, W. P., Zhang, Z.-W., & Hu, J.-Y. 2005, ApJ, 624, 808
Lee, J.-E., Bergin, E. A., & Evans, N. J., II 2004, ApJ, 617, 360
Lefloch, B., & Lazareff, B. 1994, A&A, 289, 559
Li, H., Li, D., Qian, L., et al. 2015, ApJS, 219, 20
Liu, H.-L., Wu, Y., Li, J., et al. 2015, ApJ, 798, 30
Liu, T., Wu, Y., Mardones, D., et al. 2014, PKAS, 30, 79L
Liu, T., Wu, Y., & Zhang, H. 2013, ApJL, 775, L2
Liu, T., Wu, Y., & Zhang, H. 2012a, ApJS, 202, 4
Liu, T., Wu, Y., Zhang, H., & Qin, S.-L. 2012b, ApJ, 751, 68
Machida, M. N., Inutsuka, S., & Matsumoto, T. 2008, ApJ, 676, 1088
Maddalena, R. J., & Morris, M. 1987, ApJ, 323, 179
Mardones, D., Myers, P. C., Tafalla, M., et al. 1997, ApJ, 489, 719
Mathieu, R. D. 2008, in Handbook of Star Forming Regions Vol. I, ed. B. Reipurth (San Francisco, CA: ASP), 757
Meng, F., Wu, Y., & Liu, T. 2013, ApJS, 209, 37
Morata, O., Palau, A., González, R. F., et al. 2015, ApJ, 807, 55
Morgan, L. K., Figura, C. C., Urquhart, J. S., et al. 2010, MNRAS, 408, 157
Ohashi, S., Tatematsu, K., Choi, M., et al. 2014, PASJ, 66, 119
Ogura, K. 2010, ASInC, 1, 190
Ossenkopf, V., & Henning, T. 1994, A&A, 291, 943
Palau, A., Zapata, L. A., Rodríguez, L. F., et al. 2014, MNRAS, 444, 833
Pelletier, G., & Pudritz, R. E. 1992, ApJ, 394, 117
Petriella, A., Paron, S., & Giacani, E. 2010, A&A, 513, A44
Planck Collaboration, Ade, P. A. R., Aghanim, N., Arnaud, M., et al. 2011, A&A, 536, 23
Planck Collaboration, Ade, P. A. R., Aghanim, N., Arnaud, M., et al. 2015, arXiv:150201599P
Polychroni, D., Schisano, E., Elia, D., et al. 2013, ApJL, 777, L33
Pomarès, M., Zavagno, A., Deharveng, L., et al. 2009, A&A, 494, 987
Price, D. J., Tricco, T. S., & Bate, M. R. 2012, MNRAS, 423, L45
Qiu, K., Zhang, Q., Wu, J., et al. 2009, ApJ, 696, 66
Roberts, H., Fuller, G. A., Millar, T. J., et al. 2002, A&A, 381, 1026
Robitaille, T. P., Whitney, B. A., Indebetouw, R., & Wood, K. 2007, ApJS, 169, 328
Robitaille, T. P., Whitney, B. A., Indebetouw, R., Wood, K., & Denzmore, P. 2006, ApJS, 167, 256
Sanhueza, P., Jackson, J. M., Foster, J. B., et al. 2012, ApJ, 756, 60
Sault, R. J., Teuben, P. J., & Wright, M. C. H. 1995, in ASP Conf. Ser. 77, Astronomical Data Analysis Software and Systems IV, ed. R. A. Shaw, H. E. Payne, & R. A. Hayes (San Francisco, CA: ASP), 433
Schlafly, E. F., Green, G., Finkbeiner, D. P., et al. 2014, ApJ, 786, 29
Shan, W., Yang, J., Shi, S., et al. 2012, ITTST, 2, 593
Shirley, Y. L. 2015, PASP, 127, 299
Shu, F., Najita, J., Ostriker, E., et al. 1994, ApJ, 429, 781
Solomon, P. M., Sanders, D. B., & Scoville, N. Z. 1979, in Proc. IAU Symp. 84, The Large-scale Characteristics of the Galaxy, ed. W. B. Burton (Dordrecht: Reidel), 35
Stutz, A. M., Tobin, J. J., & Stanke, T. 2013, ApJ, 767, 36
Sugitani, K., Fukui, Y., & Ogura, K. 1991, ApJS, 77, 59
Sugitani, K., & Ogura, K. 1994, ApJS, 92, 163
Thompson, M. A., Urquhart, J. S., Moore, T. J. T., et al. 2012, MNRAS, 421, 408
Thompson, M. A., White, G. J., Morgan, L. K., et al. 2004, A&A, 414, 1017
Tobin, J. J., Stutz, A. M., & Megeath, S. T. 2015, ApJ, 798, 128
Tóth, L. V., Marton, G., Zahorecz, S., et al. 2014, PASJ, 66, 17
Urquhart, J. S., Thompson, M. A., Morgan, L. K., & White, G. J. 2004, A&A, 428, 723
Urquhart, J. S., Thompson, M. A., Morgan, L. K., & White, G. J. 2006, A&A, 450, 625
Urquhart, J. S., Thompson, M. A., Morgan, L. K., et al. 2007, A&A, 467, 1125

Van der Tak, F. F. S., Black, J. H., Schöier, F. L., Jansen, D. J., & van Dishoeck, E. F. 2007, A&A, 468, 627
Wang, K., Zhang, Q., Testi, L., et al. 2014, MNRAS, 439, 3275
Wardle, M., & Königl, A. 1993, ApJ, 410, 218
Whitworth, A. P., Bhattal, A. S., Chapman, S. J., et al. 1994, MNRAS, 268, 291
Whitworth, A. P., & Zinnecker, H. 2004, A&A, 427, 299
Wu, Y., Liu, T., Meng, F., et al. 2012, ApJ, 756, 76
Yen, H.-W., Koch, P. M., & Takakuwa, S. 2015, ApJ, 799, 193
Yıldız, U. A., Kristensen, L. E., van Dishoeck, E. F., et al. 2015, A&A, 576, 109
Zavagno, A., Deharveng, L., Comerón, F., et al. 2006, A&A, 446, 171
Zavagno, A., Pomarès, M., Deharveng, L., et al. 2007, A&A, 472, 835
Zhang, C. Y., Laureijs, R. J., Chlewicki, G., et al. 1989, A&A, 218, 231
Zhang, Q., Ho, P. T. P., Wright, M. C. H., et al. 1995, ApJL, 451, L71
Zhang, Q., Wang, K., Lu, X., et al. 2015, ApJ, 804, 141
Zhou, S., Evans, N. J., II, Koempe, C., & Walmsley, C. M. 1993, ApJ, 404, 232